land

MDPI

Article

Predicting Landslide Deposit Zones: Insights from Advanced Sampling Strategies in the Ilopango Caldera, El Salvador

Laura Paola Calderon-Cucunuba [1], Abel Alexei Argueta-Platero [1,2], Tomás Fernández [3], Claudio Mercurio [1], Chiara Martinello [1], Edoardo Rotigliano [1] and Christian Conoscenti [1,*]

[1] Dipartimento di Scienze della Terra e del Mare (DiSTeM), University of Palermo, Via Archirafi 22, 90123 Palermo, Italy; laurapaola.calderoncucunuba@unipa.it (L.P.C.-C.); abel.argueta@ues.edu.sv (A.A.A.-P.); claudio.mercurio@unipa.it (C.M.); chiara.martinello@unipa.it (C.M.); edoardo.rotigliano@unipa.it (E.R.)

[2] Escuela de Posgrado y Educación Continua, Facultad de Ciencias Agronómicas, University of El Salvador, Final de Av. Mártires y Héroes del 30 Julio, San Salvador 1101, El Salvador

[3] Department of Cartographic, Geodetic and Photogrammetric Engineering, Centre for Advanced Studies in Earth Sciences, Energy and Environment. University of Jaén, 23071 Jaén, Spain; tfernan@ujaen.es

* Correspondence: christian.conoscenti@unipa.it

Abstract: In landslide susceptibility modeling, research has predominantly focused on predicting landslides by identifying predisposing factors, often using inventories primarily based on the highest points of landslide crowns. However, a significant challenge arises when the transported mass impacts human activities directly, typically occurring in the deposition areas of these phenomena. Therefore, identifying the terrain characteristics that facilitate the transport and deposition of displaced material in affected areas is equally crucial. This study aimed to evaluate the predictive capability of identifying where displaced material might be deposited by using different inventories of specific parts of a landslide, including the source area, intermediate area, and deposition area. A sample segmentation was conducted that included inventories of these distinct parts of the landslide in the hydrographic basin of Lake Ilopango, which experienced debris flows and debris floods triggered by heavy rainfall from Hurricane Ida in November 2009. Given the extensive variables extracted for this evaluation (20 variables), the Induced Smoothed (IS) version of the Least Absolute Shrinkage and Selection Operator (LASSO) methodology was employed to determine the significance of each variable within the datasets. Additionally, the Multivariate Adaptive Regression Splines (MARS) algorithm was used for modeling. Our findings revealed that models developed using the deposition area dataset were more effective compared with those based on the source area dataset. Furthermore, the accuracy of models using deposition area data surpassed that of that using data from both the source and intermediate areas.

Keywords: sampling strategies; deposit areas; debris flows; debris floods; variable significance; landslide inventory

check for updates

Academic Editor: Faccini Francesco

Received: 3 December 2024
Revised: 5 January 2025
Accepted: 22 January 2025
Published: 27 January 2025

Citation: Calderon-Cucunuba, L.P.; Argueta-Platero, A.A.; Fernández, T.; Mercurio, C.; Martinello, C.; Rotigliano, E.; Conoscenti, C. Predicting Landslide Deposit Zones: Insights from Advanced Sampling Strategies in the Ilopango Caldera, El Salvador. *Land* **2025**, *14*, 269. https://doi.org/10.3390/land14020269

Copyright: © 2025 by the authors. Licensee MDPI, Basel, Switzerland. This article is an open access article distributed under the terms and conditions of the Creative Commons Attribution (CC BY) license (https://creativecommons.org/licenses/by/4.0/).

1. Introduction

Landslide susceptibility modeling aims at assessing the probability of a landslide occurring in a given area [1,2]. This is typically achieved by creating inventories of past landslides and establishing statistical relationships between the landslide locations and the spatial variability of geo-environmental variables, such as the slope angle, elevation, lithology, and land cover [3].

The modeling of landslide susceptibility strongly depends on the chosen mapping unit, which usually corresponds to raster cells or slope units [4]. Moreover, the selection of

landslide pixels for the analysis can influence the performance of landslide susceptibility models when using raster cells. Different approaches to the selection of landslide pixels have been used in the literature, namely, (a) sampling a given number or percentage of pixels across the entire landslide area, (b) sampling pixels from the scarp zone, (c) selecting the centroid of the scarp, (d) selecting the centroid of the entire landslide area, and (e) sampling pixels within a certain buffer around the area to reproduce the pre-failure topography.

Most studies concentrated on predicting the initial conditions where the landslide started [5–9]. Some research explored whether using different parts of the landslides to train and test the models could impact their reliability and accuracy [10–13]. Magliulo et al. (2008) [11] and Regmi et al. (2014) [12] divided the landslide areas into the source and entire mass, where they obtained better results on models created with sampling on source areas and revealed that polygonal representations produced more accurate models. On the other hand, Vorpahl et al. (2021) [13] took a different approach by distinguishing between three distinct landslide areas: initiation, transport, and deposition zones. They found that models that predicted deposition areas had a better statistical significance than those that predicted initiation zones. In contrast, Vargas-Cuervo et al. (2019) [9] evaluated the difference between the highest point of the landslide and the source area (highest 10% landslide area), where they discovered superior results when focusing on the highest point (Landslide Identification Point (LIP)). Conoscenti et al. (2015) [14] emphasized that employing varied sample strategies for training models leads to significantly different landslide prediction outcomes. They suggested that preferential consideration should be given to scarps and zones uphill from crowns over landslide bodies.

Recent studies demonstrated the effectiveness of associating landslide-triggering conditions with the highest point along the crown (LIP) to develop accurate susceptibility models [10,15,16]. However, serious damage due to mass movements often occurs when the displaced material reaches areas where urban centers and economic activities are located. Consequently, if the topographic characteristics in the initiation zone differ significantly from those in the deposit zones, it raises the inference that models exclusively utilizing the LIP may not accurately predict areas where the displaced material is likely to arrive.

This study built upon existing research in landslide susceptibility modeling by exploring the prediction of landslide deposition zones, a crucial aspect for effective risk management and land-use planning. While previous studies investigated the performance of models trained and tested on the same parts of landslides, our research extended this approach by examining the cross-applicability of models trained on one landslide component and tested on another.

In addition, our study investigated four sampling strategies that captured the spatial distribution of landslide material across the source, transport, and deposition zones. By integrating these sampling strategies with the Induced Smoothed (IS) version of the Least Absolute Shrinkage and Selection Operator (LASSO) methodology, we aimed to identify the key environmental factors controlling landslide deposition and generate accurate predictions of deposit zones.

This research focused on a drainage basin in the northern sector of the Ilopango Caldera, El Salvador, which was significantly affected by Hurricane Ida in November 2009. We employed the IS-LASSO methodology for variable selection, coupled with the Multivariate Adaptive Regression Splines (MARS) algorithm for modeling landslide susceptibility.

This approach offers additional insights into the transferability of landslide susceptibility models across different landslide components, complementing existing knowledge in the field. By addressing these aspects, this study aimed to contribute to the advancement of landslide susceptibility modeling, particularly in the context of debris flows and debris floods.

The primary objectives of this research were (i) to evaluate the efficacy of models constructed using inventories of the highest point (MAX) and the highest part (SUP, which represented the top 10% of the landslide area) when predicting the entire landslide area, with particular emphasis on their ability to forecast depositional zones, and (ii) to determine the most valuable variables for accurately predicting landslide-prone areas across different landslide zones, with a focus on the cross-applicability of models trained on one zone to predict another.

2. Study Area

The study area was a basin located in the northern sector of the Ilopango caldera, which drains into the Ilopango Lake (Figure 1). The Ilopango caldera is part of the El Salvador Volcanic Front [17,18], which is related to the subduction of the Cocos plate underneath the Caribbean plate [19,20]. The eastward motion of the Caribbean plate is responsible for the transtensional deformation known as the El Salvador Fault Zone (ESFZ) [21]. This zone has dextral faults connected by pull-apart basins along fault step-overs [19,22–25] and has enabled the development of volcanic and tectonic landforms, such as strike-slip faults, normal faults, stratovolcanoes, domes, maars, and calderas [23,26].

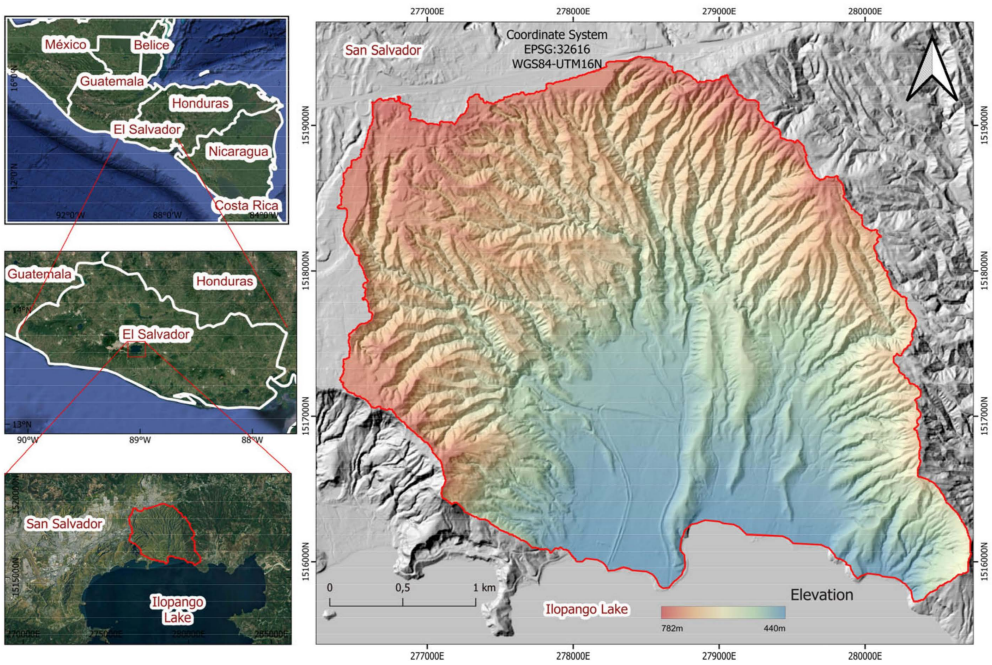

Figure 1. A northern basin of Ilopango Lake, El Salvador.

The lithology of the Ilopango area mainly consists of volcanic rocks (tuff dacitic–rhyolitic) that were deposited during the caldera-forming Quaternary explosive eruptions and are grouped into three formations, namely, the Comalapa Formation (1.78–1.32 Ma), Altavista Formation (918–257 ka), and Tierras Blancas Formation (<57 ka) [27]. From south to north, alluvial deposits, Comalapa Formation rocks (tuff), and Tierras Blancas Formation (tuff) crop out in the study area [27] (Figure 2).

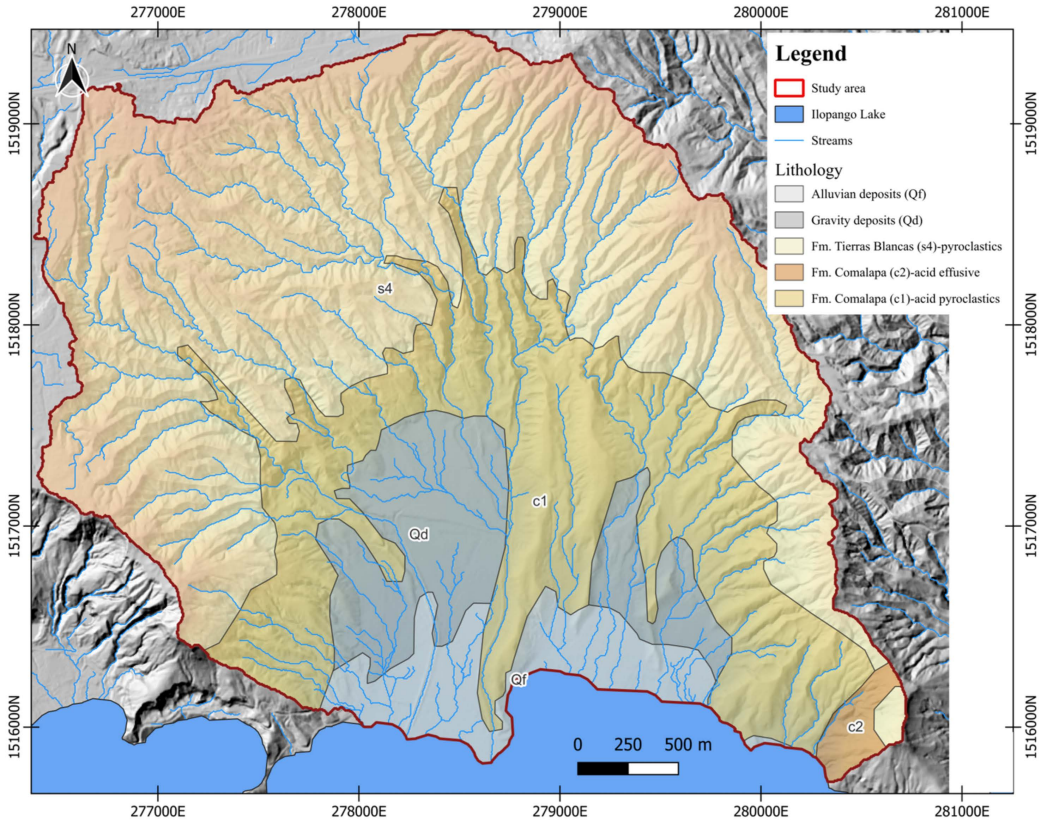

Figure 2. Lithologic map of the study area. The map illustrates the geological composition of the study area, featuring pyroclastic rocks from Formation Tierra Blanca (s4) in the upslope, and Formation Comalapa (c1) in the middle slope. In the gentile and plain areas, alluvial deposits (Qf) and gravity deposits (Qd) are predominantly present.

Since El Salvador is in the Intertropical Convergence Zone (ITCZ), it does not experience large temperature fluctuations throughout the year. The temperature mainly depends on the altitude, although it slightly increases during March and April, while it decreases during December and January [28]. The rainy season runs from May to October and the dry season from November to April. The national precipitation annual average is 1863 mm (1981–2010 series). The coasts and interior valleys are considered relatively dry (1600 mm per year), and the mountain ranges and volcanoes are considered humid (2400 mm per year). Given its location in the ITCZ, meteorological disturbances can occur from June to November, generating low-intensity precipitation that produces significant amounts of rain. The maximum rainfall records generally occur in June and September, reaching approximately 350 mm per month [28].

From November 4th to 10th of 2009, a hurricane called Ida crossed Central American countries. During its passage through El Salvador, the hurricane produced torrential rainfalls that caused significant flooding and many landslides, which resulted in a significant loss of life and property. Figure 3 reveals the magnitude of the landslides and flooding that occurred in the study area after Hurricane Ida.

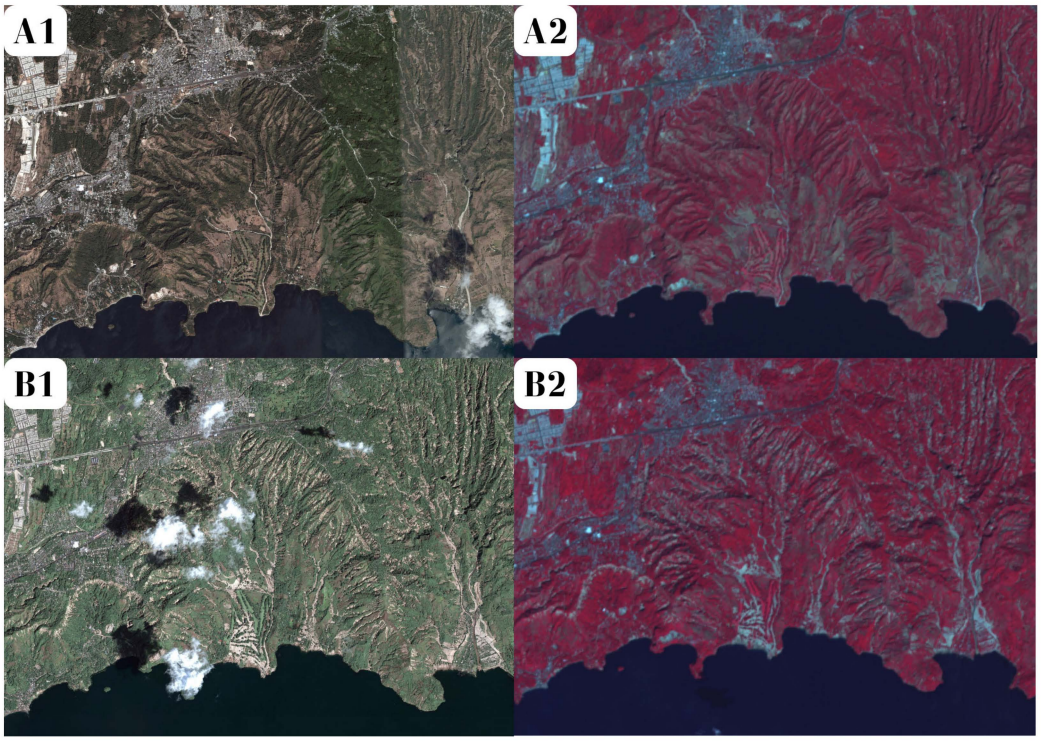

Figure 3. (**A1**,**A2**) Natural-color and false-color images from February 2009 (before the hurricane). (**B1**,**B2**) Natural-color and false-color images from November 2009 (after the hurricane). Source: Natural-color imagery obtained via Google Earth by Maxar Technologies; false-color imagery obtained via Google Earth Engine using data from the Aster sensor.

3. Materials and Methods

3.1. Landslide Mapping

A catalog of the landslides caused by Hurricane Ida within the area of interest was prepared by the visual interpretation of Google Earth imagery. Each slope failure in the inventory was digitized as a vector polygon that included the initiation, transport, and deposition zone. The landslides were detected according to the diagnostic criteria outlined by Rabby et al. (2019) [29]. These were related to the vegetation changes, morphological alterations, and the presence of debris at the base of suspected areas. To assess the vegetation changes, pre- and post-Hurricane Ida Google Earth imagery was compared. Areas that exhibited a significant loss of vegetation cover, where healthy vegetation was replaced by bare ground, were identified as potential landslide locations. Additionally, morphological alterations, such as the formation of new scarps, the deposition of debris, and changes in drainage patterns, were observed. The presence of debris deposits located downslope from suspected areas further corroborated the identification of landslides.

3.2. Independent Variables

The stochastic modeling of landslide susceptibility requires a suite of geo-environmental variables that represent factors assumed to influence the slope stability. The selection of the landslide predictors is typically based on findings from previous research, where the control of these variables on landslide spatial distribution was demonstrated (e.g., [14,30,31] and references therein). This selection is also constrained by data availability, ensuring that the chosen predictors can be accurately mapped and incorporated into the analysis. Once the relevant predictive variables have been identified, statistical or machine learning methods are employed to estimate the probability of future landslide occurrences. This is based on

the establishment of relationships identified between the spatial distribution of observed landslides and the variability of the predictors [14].

In this study, 19 topographic attributes derived from a Digital Elevation Model (DEM) were employed as predictors of the landslide distribution (Table 1). The DEM was generated by resampling a LiDAR-derived DEM provided by the Ministry of Environment and Natural Resources (MARN) of El Salvador to a 5 m resolution. The topographic attributes were subsequently calculated from the resampled DEM using the open-source SAGA-GIS 9.5.1 software [32].

Additionally, outcropping lithology and vegetation cover in the area prior to the landslide event were included as predictor variables. The lithological units were extracted from the General Geological Map of El Salvador at a scale of 1:500,000 [33], which are represented in the area shown in Figure 2 and summarized in Table 2.

The vegetation cover prior to the landslide event was assessed by calculating the Normalized Difference Vegetation Index (NDVI) from Aster images of February 2009 available on the Google Earth Engine (GEE) platform. These images include the red and near-infrared (NIR) bands required for the NDVI calculation, which were determined as the difference between the NIR and red bands divided by their sum (Equation (1)). NDVI values range from −1 to 1, with values closer to 1 indicating healthy vegetation, while values near the lower bound (typically close to zero or negative) signify non-vegetated areas, such as soil. Healthy vegetation absorbs red light strongly and reflects near-infrared light substantially, resulting in high NDVI values [34,35].

$$\mathrm{NDVI} = \frac{\mathrm{NIR} - \mathrm{red}}{\mathrm{NIR} + \mathrm{red}} \tag{1}$$

Using the Google Earth Engine (GEE) code editor, available satellite images were accessed and identified, with filters applied based on both the date and geographical area. The computation of the Normalized Difference Vegetation Index (NDVI) involved performing an algebraic operation within the GEE JavaScript programming environment. Specifically, band 3N (NIR) and band 02 (red) from the Aster satellite images were utilized. Subsequently, the resulting NDVI image, which represented the vegetation conditions before the hurricane, was exported in "GeoTIFF" format for further analysis. Since the original pixel size was 15 m, resampling was performed to reduce it to 5 m, aligning the resolution with the DEM extraction variables (see Table 1). This process ensured that the NDVI image had the same pixel dimensions and spatial alignment as the geo-environmental variables extracted from the DEM.

Table 1. Topographic attributes.

Variable Name	Abbreviation	Description
Elevation	ELE	Altitude in meters.
Slope	SLO	Maximal rate of change of elevation values between horizontal and tangential planes [36].
Plan curvature	PCV	Convergence and divergence of a normal section on the surface [37].

Table 1. *Cont.*

Variable Name	Abbreviation	Description
Profile curvature	PRC	Relative deceleration or acceleration of flow according to a profile plane that cuts the surface [38].
Longitudinal curvature	LCV	The intersection between the normal surface plane and the direction of the maximum gradient [36].
Maximal curvature	MXC	Maximal value of the normal section curvature [39].
Minimal curvature	MNC	Minimal value of the normal section curvature [39].
Tangential curvature	TNC	Convex and concave shapes of a horizontal plane [40].
Convergence index	CVI	Smoother plan curvature outcomes [41,42].
Cross-sectional curvature	CROSS	Intersection of the normal surface with the maximum gradient direction [36].
LS factor	LSF	Slope length using the slope gradient and the slope length factor (RUSLE) [43].
Relative slope position	RSP	Define the surface in values ranging from downslope near zero (channel lines) to upslope upper values (ridge lines) [42,44].
Stream power index	SPI	Flow erosion potential, considering the amount of water contributed by the upslope area and the velocity of the water flow [45].
Topographic wetness index	TWI	Water accumulation tendency based on the specific catchment area and the local slope angle [46].
Terrain ruggedness index	TRI	Measures the terrain heterogeneity between a grid cell and its eight neighbor grid cells [47].
Topographic position index	TPI	Classification of the landscapes into slope position classes [48].
Vertical distance to channel network	VDCN	It constitutes a theoretical surface regarding the channel lines ("base level") [49].
Northness	N	Cosine of slope aspect.
Eastness	E	Sine of slope aspect.

Table 2. Lithology classes.

Variable Name	Abbreviation	ID	Model ID	Description
Lithology	LITO	1	LTL1	Fm. Comalapa (c2)—acid pyroclastic
		2	LTL2	Fm. Comalapa (c1)—acid effusive
		3	LTL3	Fm. Tierras Blancas (s4)—pyroclastics
		4	LTL4	Alluvial deposits (Qf)
		5	LTL5	Gravity deposits (Qd)

3.3. Dependent Variable

To investigate the relationship between the predictors and landslide locations, a 5 m grid cell was chosen as the mapping unit. This resolution corresponds to that of the DEM employed in the analysis.

The dependent variable, which represented the landslide occurrence, was defined as a binary categorical variable at the cell level. Cells that intersected landslide polygons were assigned a value of 1, indicating the presence of a landslide, while cells that did not intersect any landslide polygons were assigned a value of 0, indicating stability.

To assess the influence of landslide cells selection on model performance, the predictive models were calibrated and validated using four distinct datasets. The datasets, which were named MAX, SUP, INF, and BODY, comprised landslide cells extracted from different portions of the landslide polygons (Figure 4). The MAX dataset included the highest elevation cell within each landslide polygon. This selection strategy aimed to represent the environmental conditions prevalent at the landslide initiation points, where failure is typically triggered. The SUP dataset included a random selection of the highest 10% of cells within each landslide polygon, with the aim to characterize the environmental conditions prevalent in the main source areas. Conversely, the INF dataset comprised a random selection of the lowest 10% of cells, which were expected to be representative of the accumulation zones. The BODY dataset comprised a random selection of cells within each landslide polygon, with the aim to represent the environmental conditions across the entire landslide area.

This study differentiated between two distinct types of mass-wasting phenomena: debris flows and debris floods. These phenomena exhibit distinct characteristics in terms of their initiation mechanisms, flow dynamics, and depositional patterns [50]. Debris flows typically exhibit a more confined and channelized form, with a relatively short distance between the source area and the accumulation zone. Conversely, debris floods are characterized by a more widespread and diffuse pattern of deposition, often encompassing significantly larger areas and exhibiting a greater distance between the source and accumulation zones (Figure 5). Thus, to account for their different characteristics, the four strategies of landslide cell selection were applied to each phenomenon type, which resulted in a total of eight datasets.

Since different landslides are employed for model calibration and validation, and considering that landslide polygons exhibit considerable variability in size, a standardized sampling strategy was implemented to mitigate the potential bias. Specifically, the maximum number of pixels extracted from each landslide polygon to construct the SUP, INF, and BODY datasets of both the debris flows and floods was held constant. This approach ensured that larger landslides did not disproportionately influence the size of the training and testing samples, thereby promoting a more balanced and robust assessment of the model performance. In the case of the debris flow inventory, a maximum of 2 pixels was randomly sampled to represent both the SUP and INF portions of each landslide, while the BODY dataset incorporated up to a maximum of 8 random pixels. Conversely, for the debris flood inventory, which generally encompasses larger landslide areas, the SUP and INF portions were represented by a maximum of 7 pixels each, and the BODY dataset included up to a maximum of 63 pixels.

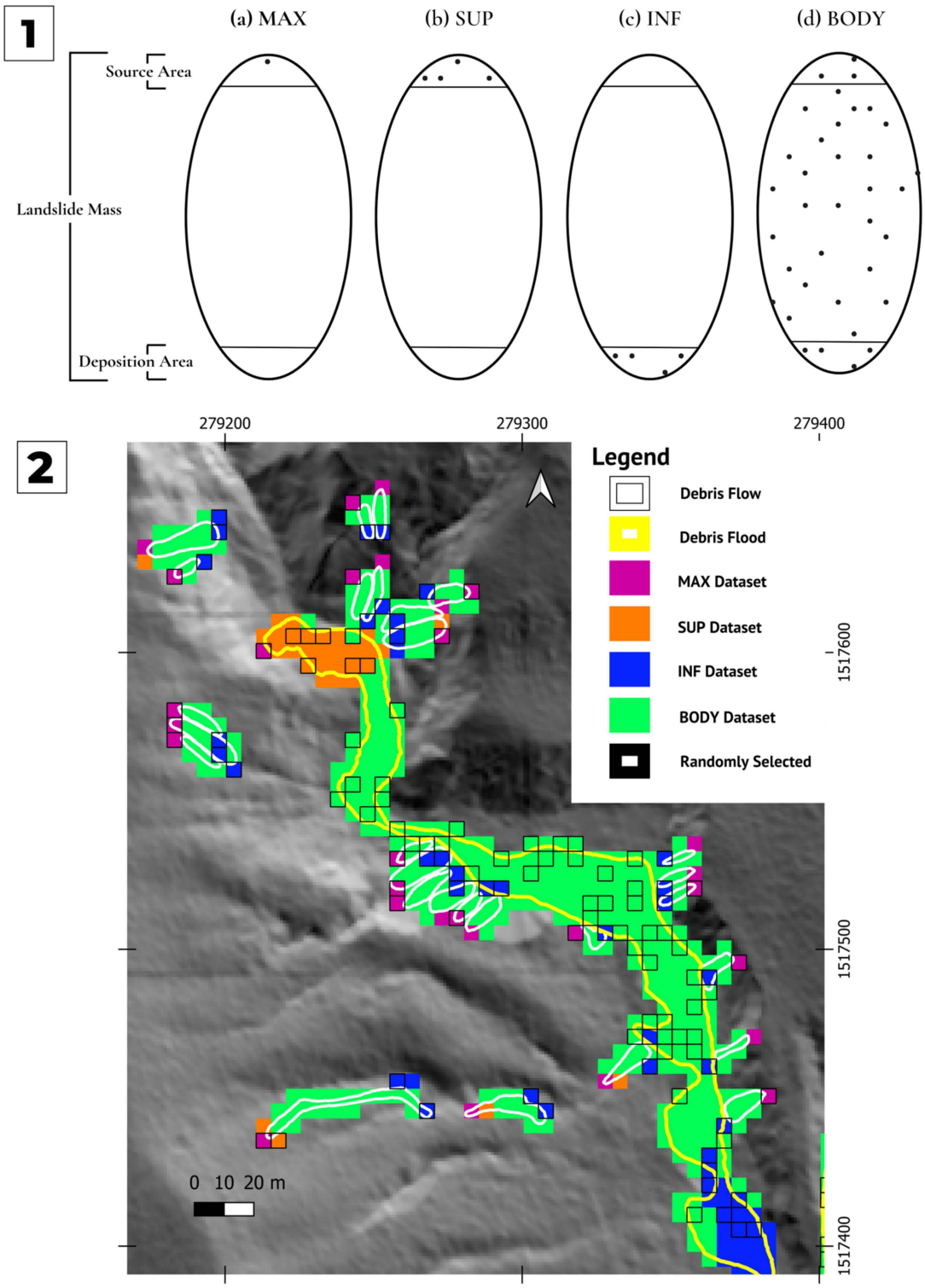

Figure 4. Illustration of the four different approaches adopted for selecting cells within a landslide polygon: (**1**) a conceptual representation and (**2**) the actual subdivision in the dataset. The approaches were (**1a**) MAX: the cell with the highest elevation; (**1b**) SUP: randomly selected cells from the upper 10% of the landslide area; (**1c**) INF: randomly selected cells from the lower 10% of the landslide area; and (**1d**) BODY: randomly selected cells from across the entire landslide area.

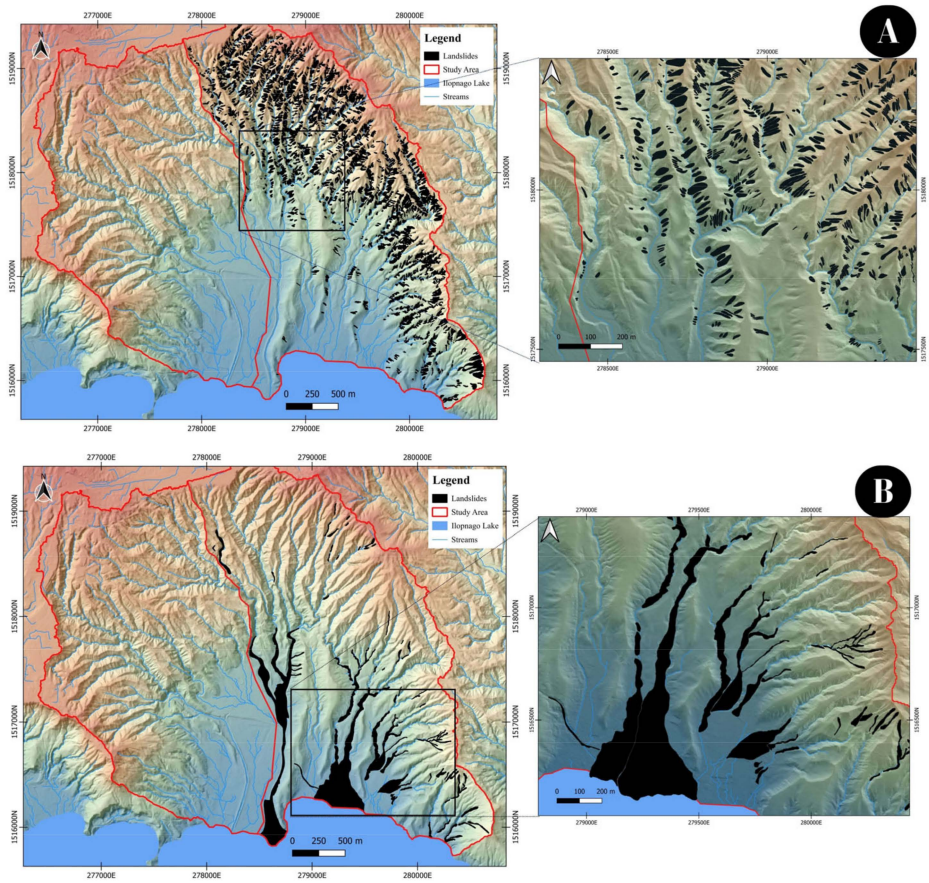

Figure 5. Landslides inventories. (**A**) "Debris Flow" dataset, which comprised landslides with similar geometries and sizes. (**B**) "Debris Flood" dataset, characterized by extensive deposit areas.

3.4. Univariate Analysis of Variables

The process began with testing an extensive array of geo-environmental variables on each dataset. The variable analysis was conducted using the Induced Smoothed (IS) version of the Least Absolute Shrinkage and Selection Operator (lasso) method, which focuses on hypothesis testing. The IS-lasso assesses the statistical significance of the regression coefficients of large groups of predictors, aiding in the acquisition of an appropriate covariance matrix and Wald statistic with relative ease [51]. This method facilitates the estimation of the covariate effect by providing point estimates and reliable standard errors for computing confidence intervals and *p*-values [51]. In this context, the use of *p*-values under the threshold of 0.05 assists in determining whether a variable is significant in predicting the landslide occurrence. The IS-lasso method was implemented using the "islasso" package within the R 4.3.1 statistical programming environment [52].

The results provided by the "islasso" package include a significance code indicated by asterisks, which help determinate the level of coefficient significance. The most significant is denoted by three asterisks, representing a level of 0.001, followed by two asterisks for a level of 0.01. A single asterisk corresponds to a level of 0.05, and a dot indicates 0.1. Additionally, if the *p*-value is zero, it signifies that the coefficient is highly significant.

3.5. Statistical Modeling

Debris flow and debris flood susceptibilities within the study area was modeled using the Multivariate Adaptive Regression Splines (MARS) algorithm.

MARS is a non-parametric regression technique that estimates general functions from high-dimensional data [53]. This algorithm extends traditional linear models by generating a series of basis functions, effectively partitioning the data into distinct intervals and fitting

separate regression models within each interval. This piecewise linear representation, connected at "knots" or breakpoints, allows for greater flexibility in capturing complex non-linear relationships between the predictors and the response variable.

The MARS algorithm employs a two-step procedure: a forward pass, where an overabundance of basis functions is generated, followed by a backward pass, where the optimal set of basis functions is selected to minimize overfitting and produce a parsimonious model [53]. This results in a smooth, continuous response curve that accurately reflects the underlying relationships in the data while maintaining interpretability [8].

The strength of MARS lies in its capacity to identify predictive relationships between a response variable and a multitude of predictor variables. This is achieved by leveraging the values of the predictor variables in the training data to construct a rule for estimating response values in test observations [53].

Model development was carried out within the R statistical programming environment using the "Earth" package [52].

3.6. Validation Strategy

The validation strategy employed in this study consisted of a random partition of the datasets previously obtained (MAX, SUP, INF, BODY) into separate calibration and validation sets [54]. To mitigate the potential influence of spatial autocorrelation, the initial step involved stratifying the landslide polygons of both the debris flow and debris flood events into distinct training and validation sets, with 75% and 25% of the polygons allocated to each set, respectively. This stratification ensured that pixels that belonged to the same landslide polygon were not included in both the training and validation sets, which prevented any artificial inflation of model performance.

Following the stratification of landslide polygons, a balanced sampling strategy was employed to extract an equal number of landslide and non-landslide cells for each training and validation set. The landslide cells comprised all pixels of each dataset within the selected landslide polygons, while an equal number of non-landslide cells were randomly sampled from stable areas located outside the landslide polygons. This balanced sampling approach ensured that the models were not biased toward predicting either the landslide or non-landslide occurrences.

Finally, a MARS model was calibrated for each training sample and subsequently applied to the corresponding validation sample to evaluate its predictive performance. This entire process, from the initial stratification of landslide polygons to the final model validation, was repeated 10 times, with different training and validation sets used in each iteration. This repetition allowed for a comprehensive assessment of the models' predictive capabilities and their robustness to variations in the training and testing data.

The model accuracy was evaluated using receiver operating characteristic (ROC) curves and the corresponding area under the ROC curve (AUC) values, calculated for both the training and testing samples. The ROC curve provides a graphical representation of the model performance across various classification thresholds, plotting the sensitivity (true positive rate) against 1-specificity (false positive rate) [55]. This visualization allows for a comprehensive assessment of the trade-offs between true positive and false positive rates at different thresholds.

The AUC, a summary measure of the overall model performance, represents the probability that the model will correctly rank a randomly chosen instance as either a landslide or non-landslide. An AUC value of 1 signifies perfect discrimination, while a value of 0.5 indicates a model with no discriminatory ability [55]. The thresholds of the AUC were used to categorize the model accuracy: models that achieved AUC values greater

than 0.7 were deemed acceptable, while those that exceeded 0.8 and 0.9 were classified as excellent and outstanding, respectively [9].

4. Results

4.1. Landslide Inventory

In the study area, we identified a total of 4,316 landslides (classified as debris flows) and 97 landslides with extensive deposits (classified as debris floods) using the November 2009 image available on Google Earth. Mostly, debris flows and debris floods occurred in this basin following the hurricane event, as illustrated in Figure 6. Debris flows are characterized by the rapid, saturated movement of significant debris material with water entrainment, leading to areas devoid of vegetation. In contrast, debris floods refer to a very rapid flow of water heavily charged with debris, comparable with the peak discharge of a water flood, as outlined by [50].

Figure 6. Landslide mapping of debris floods (**A**) and debris flows (**B**).

4.2. Variable Behavior on Each Dataset

The statistical significance of the 20 continuous variables (which excluded lithology) assessed with the IS-lasso method in each dataset is detailed in Table 3. There was a higher number of significant variables in the debris flow database compared with the databases of debris floods. In both the debris flow and flood databases, a greater selection of significant variables for predicting the occurrence of landslides was observed within the BODY subdivision, as well as MAX in the debris flows.

Table 3. *p*-values obtained by applying the IS-lasso method on each database and the importance of the variables revealed by the number of asterisks.

	Debris Flow Database								Debris Flood Database							
Variable	**MAX**	**Imp**	**SUP**	**Imp**	**INF**	**Imp**	**BODY**	**Imp**	**MAX**	**Imp**	**SUP**	**Imp**	**INF**	**Imp**	**BODY**	**Imp**
ELE	7.12×10^{-4}	***	8.33×10^{-1}		6.22×10^{-19}	***	7.68×10^{-76}	***	0.0100404	*	7.55×10^{-90}	***	5.29×10^{-50}	***	$0.00 \times 10^{+00}$	NA
SLO	3.15×10^{-19}	***	7.71×10^{-38}	***	6.68×10^{-70}	***	$0.00 \times 10^{+00}$	NA	0.091878	.	8.12×10^{-4}	***	2.22×10^{-1}		3.08×10^{-1}	
PCV	1.69×10^{-2}	*	2.16×10^{-10}	***	6.37×10^{-5}	***	5.98×10^{-9}	***	0.9999999		6.65×10^{-1}		6.55×10^{-1}		$1.00 \times 10^{+00}$	
PRC	1.45×10^{-12}	***	8.82×10^{-20}	***	1.36×10^{-1}		4.01×10^{-1}		0.9999992		$1.00 \times 10^{+00}$		$1.00 \times 10^{+00}$		$1.00 \times 10^{+00}$	
LCV	8.20×10^{-1}		2.41×10^{-1}		7.45×10^{-1}		$1.00 \times 10^{+00}$		0.9999959		6.02×10^{-3}	**	$1.00 \times 10^{+00}$		9.31×10^{-2}	.
MXC	6.26×10^{-2}	.	2.76×10^{-2}	*	5.80×10^{-5}	***	2.67×10^{-18}	***	0.9999974		5.99×10^{-1}		$1.00 \times 10^{+00}$		6.51×10^{-1}	
MNC	3.67×10^{-3}	**	3.31×10^{-10}	***	4.16×10^{-1}		1.03×10^{-23}	***	0.9999997		$1.00 \times 10^{+00}$		$1.00 \times 10^{+00}$		$1.00 \times 10^{+00}$	
TNC	$1.00 \times 10^{+00}$		$1.00 \times 10^{+00}$		7.62×10^{-1}		$1.00 \times 10^{+00}$		0.9999995		$1.00 \times 10^{+00}$		$1.00 \times 10^{+00}$		$1.00 \times 10^{+00}$	
CVI	9.56×10^{-12}	***	6.03×10^{-4}	***	6.06×10^{-43}	***	4.40×10^{-8}	***	0.0025186	**	9.03×10^{-1}		2.27×10^{-1}		4.33×10^{-6}	***
CROSS	7.03×10^{-1}		2.93×10^{-1}		$1.00 \times 10^{+00}$		$1.00 \times 10^{+00}$		0.9999983		3.75×10^{-1}		$1.00 \times 10^{+00}$		9.92×10^{-1}	
LSF	8.00×10^{-5}	***	1.79×10^{-5}	***	5.70×10^{-2}	.	4.91×10^{-2}	*	0.26371		3.19×10^{-1}		2.46×10^{-1}		3.58×10^{-5}	***
RSP	2.20×10^{-4}	***	7.38×10^{-1}		1.98×10^{-4}	***	1.86×10^{-2}	*	0.7148685		1.47×10^{-4}	***	2.17×10^{-33}	***	1.84×10^{-92}	***
SPI	3.59×10^{-2}	*	1.82×10^{-2}	*	1.72×10^{-6}	***	1.07×10^{-12}	***	0.5813285		6.89×10^{-1}		1.27×10^{-4}	***	1.37×10^{-2}	*
TWI	2.93×10^{-6}	***	7.19×10^{-11}	***	1.09×10^{-6}	***	1.59×10^{-32}	***	0.7847661		1.05×10^{-2}	*	9.79×10^{-13}	***	1.24×10^{-46}	***
TRI	8.15×10^{-20}	***	1.37×10^{-42}	***	2.38×10^{-27}	***	3.17×10^{-252}	***	0.2310383		1.54×10^{-3}	**	7.20×10^{-1}		1.11×10^{-1}	
TPI	1.94×10^{-26}	***	2.31×10^{-67}	***	2.91×10^{-125}	***	2.50×10^{-20}	***	0.9782402		3.64×10^{-37}	***	8.11×10^{-3}	**	2.56×10^{-89}	***
VDCN	8.60×10^{-1}		1.11×10^{-1}		4.84×10^{-47}	***	1.50×10^{-83}	***	0.2114126		4.18×10^{-2}	*	7.94×10^{-2}	.	1.57×10^{-22}	***
NDVI	7.46×10^{-5}	***	1.36×10^{-4}	***	1.57×10^{-3}	**	9.36×10^{-33}	***	0.9999999		3.96×10^{-7}	***	1.98×10^{-6}	***	7.92×10^{-81}	***
N	1.53×10^{-15}	***	5.96×10^{-14}	***	2.63×10^{-2}	*	2.79×10^{-6}	***	0.9038835		4.53×10^{-1}		2.27×10^{-1}		1.61×10^{-1}	
E	5.37×10^{-3}	**	8.02×10^{20}	***	1.59×10^{-14}	***	$0.00 \times 10^{+00}$	NA	0.1585544		1.99×10^{-3}	**	1.07×10^{-19}	***	4.52×10^{-85}	***

(***) 0.001: highly significant. (**) 0.01: significant. (*) 0.05: marginally significant. (.) 0.1: trend or close to significance. (NA): highly significant.

In Figure 7, the significance of each variable is revealed by the number of asterisks, which depended on the *p*-value obtained by applying the IS-lasso method to each dataset. It is evident that SLO exhibited the highest importance across all four datasets, followed by CVI, TWI, TRI, TPI, and E. Conversely, LCV, TNC, and CROSS, were not deemed significant in differentiating landslide occurrences. In the case of the BODY dataset, both the SLO and E variables showed high significance.

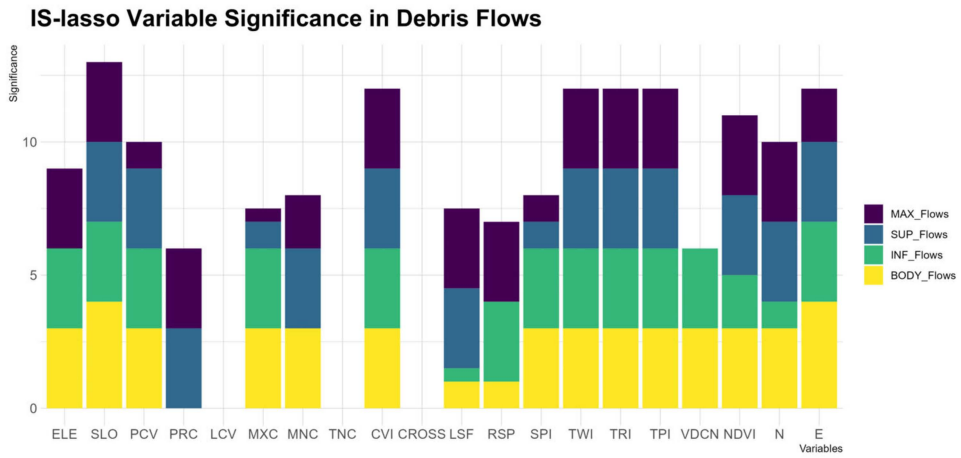

Figure 7. Significance of the variables observed on each dataset (MAX, SUP, INF, and BODY) for the debris flow database according to the IS-lasso method.

Figure 8 shows that the ELE variable held the highest significance on the BODY debris flood dataset. Only a few variables (namely, CVI, ELE, and SLO) were capable of differentiating landslide occurrences in the MAX dataset. Moreover, variables such as RSP, TWI, TPI, VDCN, NDVI, and E showed significance across the other three datasets (BODY, SUP and INF), while SLO, LCV, and CVI were significant only in two datasets. Finally, TRI and LSF were significant in just one dataset.

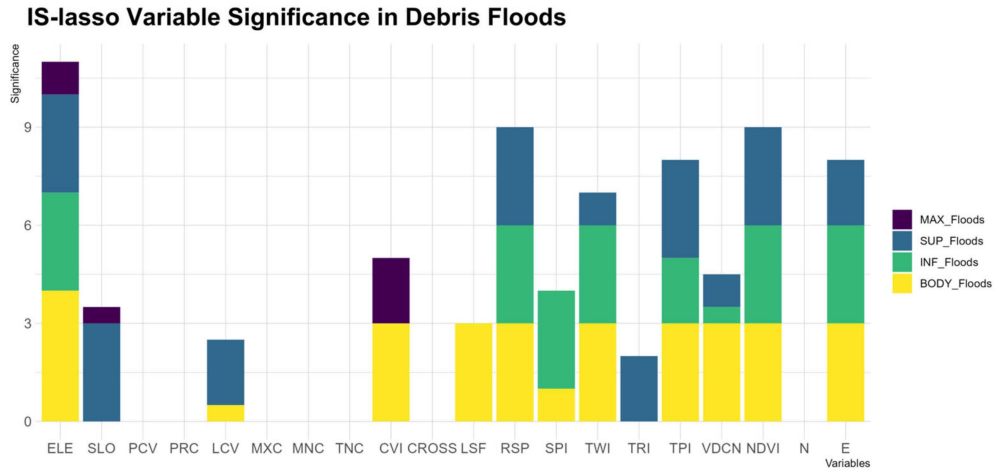

Figure 8. Significance of the variables observed on each dataset (MAX, SUP, INF, and BODY) for the debris flood database according to the IS-lasso method.

To understand the distribution of the categorical variable, lithology, the percentage of each category within the landslide areas was calculated for each database (debris flows and debris floods) (Figure 9). In the debris flow database, category "3", which corresponded to Fm. Tierras Blancas (s4), constituted the highest percentage in the area, with about 74%. It was followed by category "1" (Fm. Comapala, c2), which represented around 23% in the area. Conversely, in the debris flood database, the most representative categories were "1", "4", and "5", which corresponded to Fm. Comapala (c2), alluvial deposits (Qf), and gravity deposits (Qd), respectively. These categories had high percentages, where they represented approximately 33%, 28%, and 26% of the landslide area, respectively.

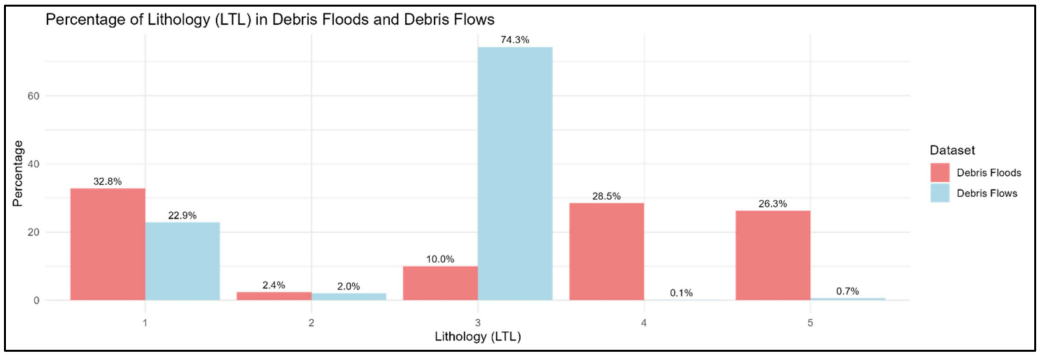

Figure 9. Percentage of each lithology category within landslide areas, calculated for the debris flow and debris flood databases. (1) Fm. Comalapa (acid pyroclastic). (2) Fm. Comalapa (acid effusive). (3) Fm. Tierras Blancas (pyroclastics). (4) Alluvial deposits. (5) Gravity deposits.

4.3. Calibration of the Models

The selection of independent variables for calibrating the landslide susceptibility models was guided by their statistical significance and relevance to the prediction of landslide cells occurrence within each of the four datasets (i.e., MAX, SUP, INF, and BODY). This approach to the variable selection ensured that each model incorporated only the most salient predictors, which enhanced the model parsimony and interpretability while maintaining the predictive accuracy.

As illustrated in Figure 7, the variables LCV, TNC, and CROSS were excluded from all debris flow models due to their lack of statistical significance in distinguishing between landslide and non-landslide areas within this inventory. Moreover, specific variables were excluded from certain datasets based on their lack of statistical significance. Specifically, VDCN was excluded from the MAX and SUP datasets, PRC from the INF and BODY datasets, RSP and ELE from the SUP dataset, and MNC from the INF dataset.

Similarly, as depicted in Figure 8, the following variables were deemed non-significant in discriminating the debris flood cells of the four datasets and were consequently excluded when calibrating the relative MARS models: PCV, PRC, MXC, MNC, TNC, CROSS, and N. Moreover, SLO and TRI were excluded from the INF and BODY models, LSF and CVI from the SUP and INF models, SPI from the SUP models, and LCV from the INF models. Notably, the MAX model, calibrated with the highest points of the debris floods, exhibited the most stringent variable selection, where only ELE, SLO, and CVI demonstrated statistical significance and was retained in the final model. This selective inclusion of variables highlights the distinct environmental controls that operated at the landslide initiation points compared with the other zones within the landslide area.

Following the identification of the most significant predictor variables, the MARS models were calibrated using the training samples, which comprised 75% of the debris flow and debris flood polygons. The calibration process enabled an assessment of variable importance by examining the mean Residual Sum of Squares (RSS) across the ten repetitions.

This metric is calculated by summing the squared differences between the observed and model-predicted values. Following the Earth package documentation [56], the importance of each variable was determined by analyzing the decrease in RSS associated with its inclusion in the model. Specifically, the decrease in the RSS for each subset of predictors was calculated relative to the preceding subset, and these decreases were summed and normalized across all subsets, with the largest decrease scaled to 100. Variables that resulted in the greatest net decrease in the RSS were deemed to have a higher importance in explaining the landslide occurrence.

According to the RSS value, in the debris flow database, the SLO variable was the most important in the MAX and SUP models, followed by LSF in the INF and BODY models, as shown in Figure 10. However, each subdivision model showed different variable importance. In the MAX model, SLO, ELE, and PRC took precedence, while in the SUP model, SLO, TPI, and TWI were significant. For the INF model, LSF, TPI, and ELE were significant, and in the BODY model, LSF, ELE, and SLO held importance. Moreover, lithology LTL3 was recognized as the fourth most significant variable in the SUP model, acting as the only categorical variable. However, in MAX, INF, and BODY, lithologies LTL2 and LTL3 were identified as among the least important variables for predicting the landslide areas.

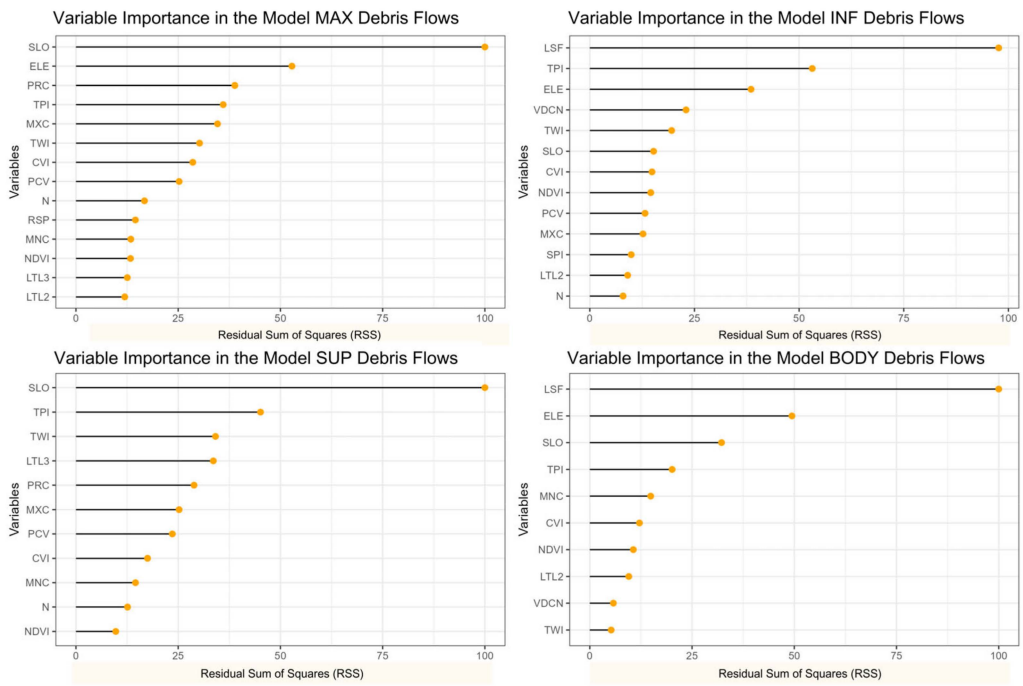

Figure 10. Variable importance scores derived from the MARS models for each debris flow dataset (MAX, SUP, INF, and BODY).

In the debris flood database, RSP was identified as the most important variable in INF and SUP, and TPI was the most important in BODY, as illustrated in Figure 11. The variable importance varied across models, with CVI, SLO, and ELE being most significant in the MAX model; RSP, TRI, and ELE in the SUP model; RSP, TWI, and TPI in INF model; and TPI, ELE, and RSP in the BODY models.

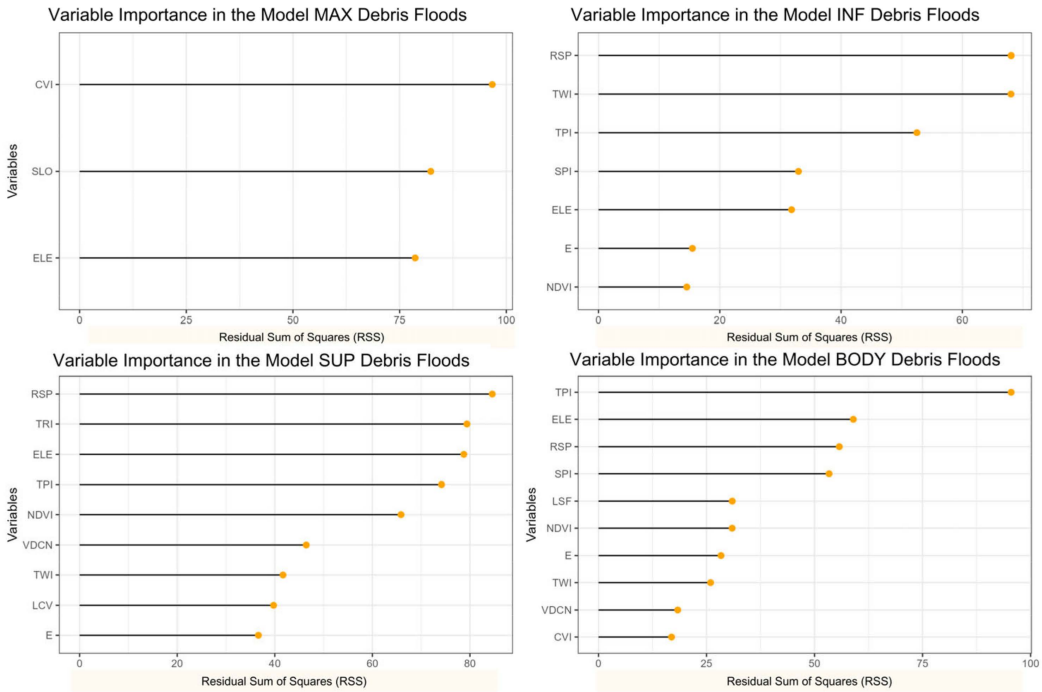

Figure 11. Variable importance scores derived from the MARS models for each debris flood dataset (MAX, SUP, INF, and BODY).

4.4. Validation of the Models

The model predictive performance was evaluated using independent validation datasets, which comprised 25% of the landslide polygons in each dataset. This evaluation simulated the prediction of future landslides and provided a robust assessment of the models' ability to accurately identify areas susceptible to mass movements.

Based on the AUC values observed for the debris flow databases, the BODY, INF, and MAX models demonstrated superior prediction accuracy when applied to the respective test datasets (Figure 12). Particularly noteworthy was the INF model, which exhibited superior performance by achieving the highest mean AUC of 0.902, with a low standard deviation of 0.0056 (Table 4). This emphasized its robust predictive capabilities for deposition areas within the INF database. Additionally, the SUP model displayed remarkable performance in predicting exclusively the highest points of landslides, particularly when applied to the MAX datasets. In contrast, the MAX model showed the lowest AUC value (0.589) when predicting deposition areas (INF database).

Regarding the debris flood database (Figure 13), the INF model outperformed the others with the highest mean AUC value of 0.913, particularly for predicting landslide areas (BODY dataset), as shown in Table 5. Notably, the BODY and INF models demonstrated statistically significant AUC values, while MAX and SUP registered values below 0.74. Additionally, the prediction of the highest part of the landslide (MAX and SUP datasets) with the BODY and INF models exhibited AUC values below 0.745, as depicted in Figure 13.

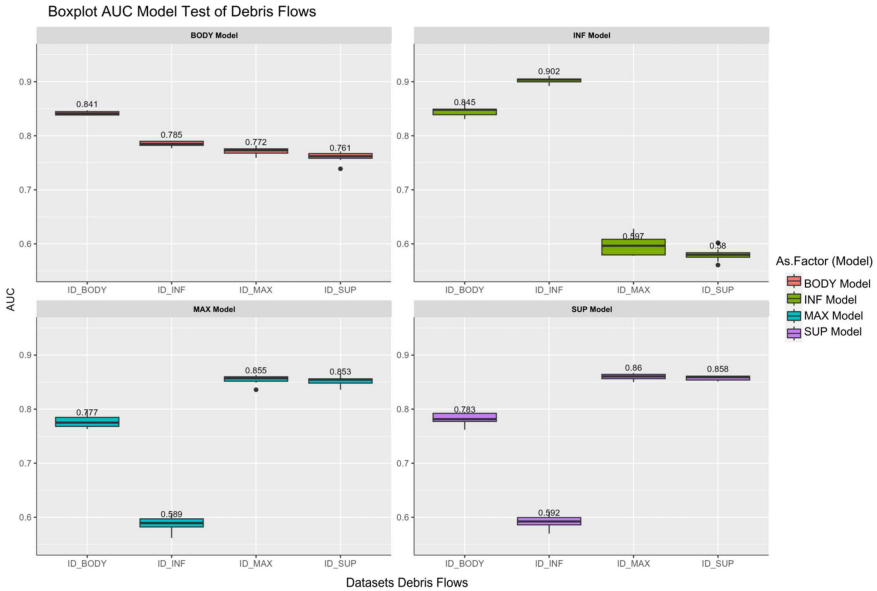

Figure 12. Boxplots depicting the distributions of the AUC values for each model (BODY, INF, MAX, and SUP) applied to the debris flow testing datasets.

Table 4. Mean and standard deviation (SD) of the AUC values derived from 10 repetitions of each model applied to the debris flow datasets.

		AUC_Test_Database_Debris Flows				AUC_Train_Database_Debris Flows			
Dataset		**BODY**	**INF**	**MAX**	**SUP**	**BODY**	**INF**	**MAX**	**SUP**
BODY Model	Mean	0.841	0.785	0.772	0.761	0.840	0.785	0.766	0.756
	SD	0.0037	0.005	0.007	0.0093	0.0014	0.0024	0.0078	0.003
INF Model	Mean	0.845	0.902	0.597	0.580	0.842	0.905	0.592	0.575
	SD	0.0095	0.0056	0.0182	0.0114	0.003	0.0023	0.0133	0.0088
MAX Model	Mean	0.777	0.589	0.855	0.853	0.780	0.591	0.864	0.855
	SD	0.0115	0.0137	0.0079	0.0086	0.0052	0.0085	0.004	0.0051
SUP Model	Mean	0.783	0.592	0.860	0.858	0.782	0.588	0.859	0.861
	SD	0.0106	0.0127	0.0052	0.0042	0.0039	0.0084	0.004	0.0031

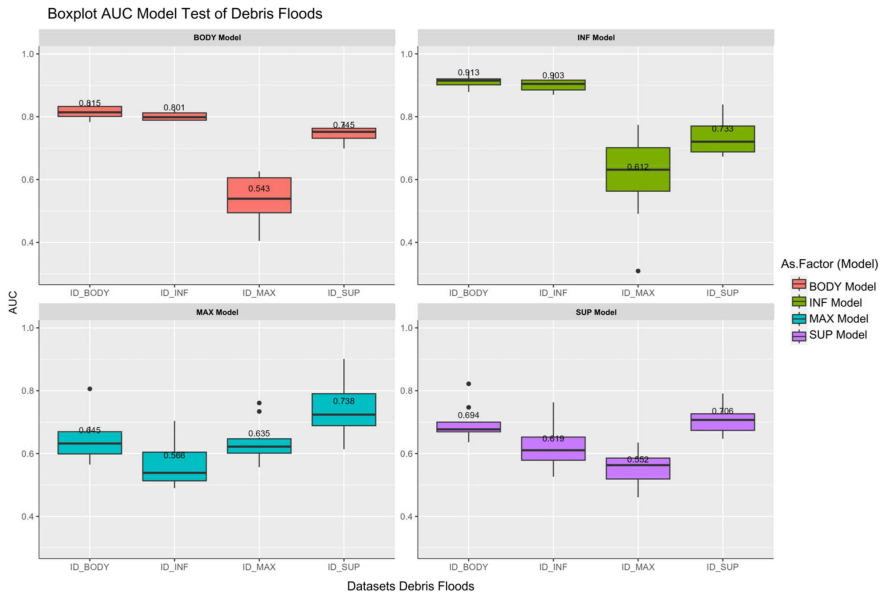

Figure 13. Boxplots depicting the distributions of the AUC values for each model (BODY, INF, MAX, and SUP) applied to the debris flood testing datasets.

Table 5. Mean and standard deviation (SD) of the AUC values derived from 10 repetitions of each model applied to the debris flood datasets.

		AUC_Test_Database_Debris Floods				AUC_Train_Database_Debris Floods			
Dataset		**BODY**	**INF**	**MAX**	**SUP**	**BODY**	**INF**	**MAX**	**SUP**
BODY Model	Mean	0.815	0.801	0.543	0.745	0.842	0.802	0.544	0.743
	SD	0.0213	0.0131	0.0725	0.0266	0.0068	0.0127	0.071	0.0129
INF Model	Mean	0.913	0.903	0.612	0.733	0.899	0.935	0.659	0.747
	SD	0.0181	0.0242	0.1369	0.0548	0.0119	0.0088	0.0942	0.0266
MAX Model	Mean	0.645	0.566	0.636	0.738	0.651	0.584	0.685	0.729
	SD	0.0685	0.07	0.0668	0.0818	0.0523	0.0357	0.068	0.069
SUP Model	Mean	0.694	0.619	0.552	0.706	0.702	0.631	0.554	0.813
	SD	0.0554	0.0678	0.0509	0.0421	0.0255	0.0281	0.0433	0.0141

4.5. Landslide Susceptibility Maps

Susceptibility maps were generated for both the landslide area (BODY) and deposition zones (INF) using the INF model trained with the debris flow database. This choice was made because the INF model demonstrated accuracies of 0.845 and 0.902 in predicting these areas for debris flows, respectively (Figure 14). Additionally, a susceptibility map for the highest part (SUP) of the landslide was created using the SUP model, which exhibited an accuracy of 0.858 (Figure 15). Furthermore, the predictions for areas susceptible to debris floods were made using the INF model, which showed an accuracy of 0.913 for the landslide area (BODY) and 0.903 for deposition zones (INF), as shown in Figure 16.

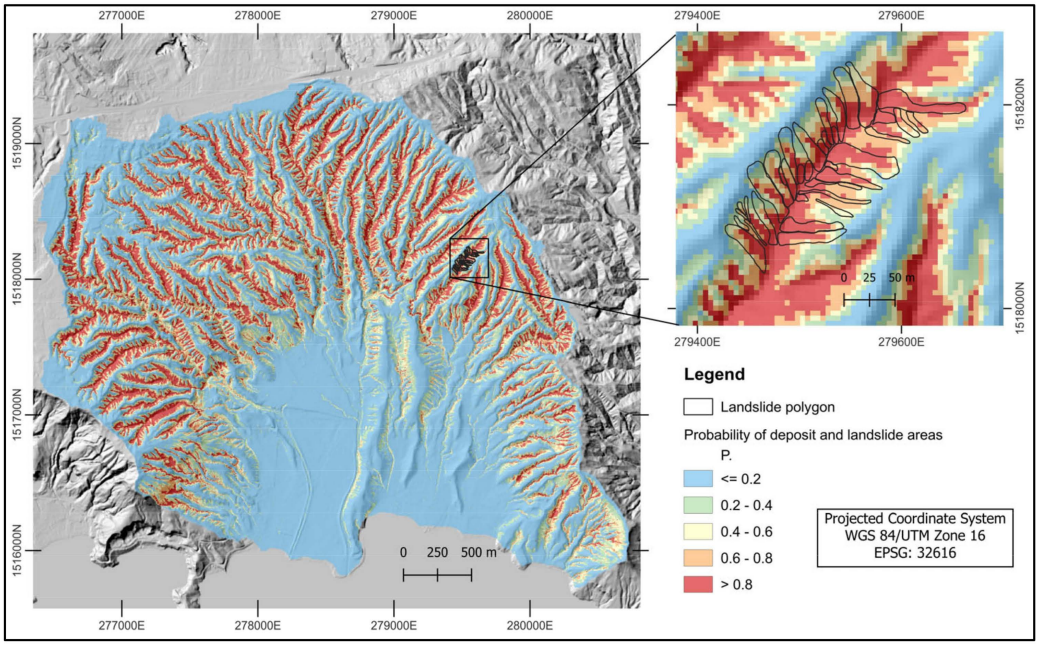

Figure 14. Susceptibility map for debris flow deposits, obtained using the INF model from the debris flow database.

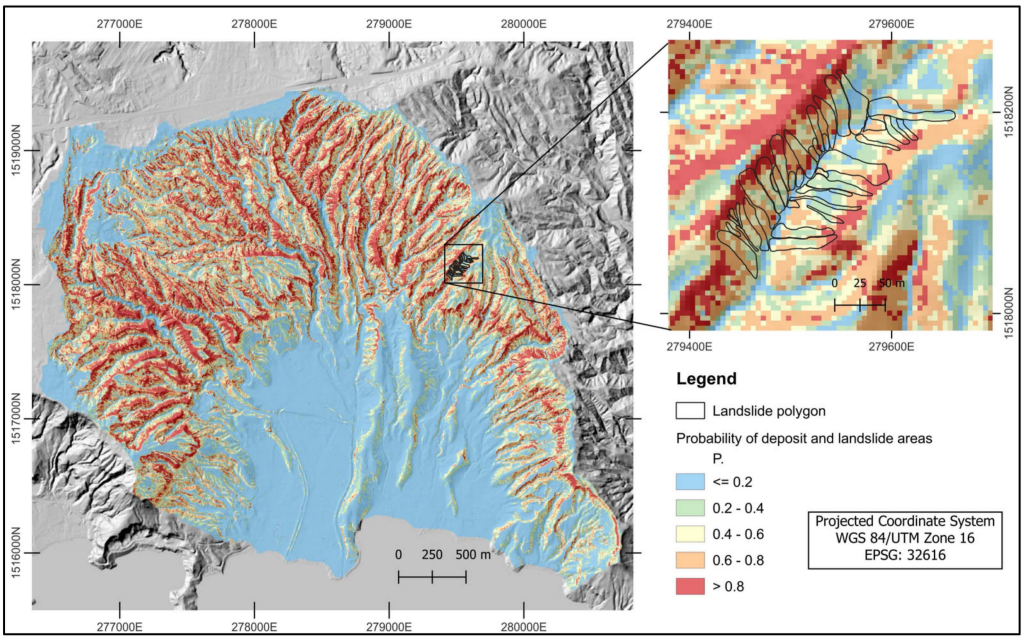

Figure 15. Susceptibility map for debris flow source areas, obtained using the SUP model from the debris flow database.

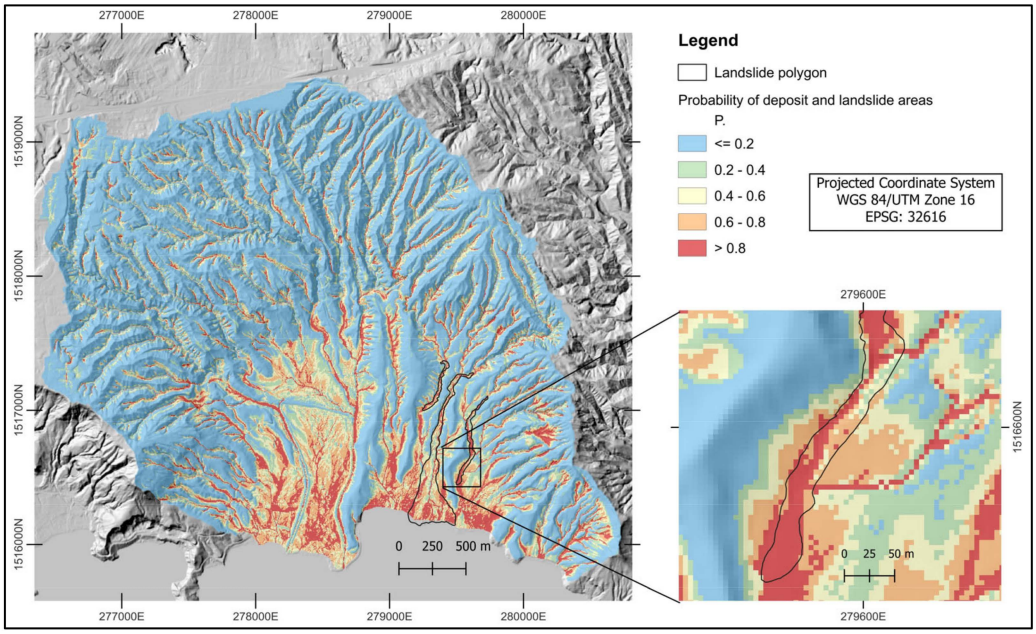

Figure 16. Susceptibility map for debris flow deposits, obtained using the INF model from the debris flood database.

5. Discussion

The primary goal of this study was twofold: first, to determine the most effective inventory, incorporating an assessment of models built with an inventory of the highest point (MAX) and the highest part (SUP), to predict landslide areas, particularly emphasizing depositional zones (INF). Second, this research aimed to identify the optimal set of variables for accurately predicting both the deposition zones and other areas affected by landslides, with a specific focus on their segmentation. This study was conducted in an area that experienced landslides triggered by rainfall during the passage of Hurricane Ida over El Salvador from 4 to 10 November 2009.

5.1. Comparing Variable Significance in IS Lasso and MARS Models

Given the extensive range of predictor variables, the application of the methodology proposed by Cilluffo et al. (2020) [51], known as "IS lasso", facilitated the identification of significant variables from a pool of 20 across each dataset. Variables with p-values < 0.05 were selected since this indicated a low probability that the observed differences were due to chance. These variables suggested statistically significant differences and enabled differentiation between the landslide and non-landslide groups.

It could be hypothesized that variables with a lower p-value would have similar statistical importance when creating the prediction model with MARS. In the case of the INF dataset related to debris flows, TPI, SLO, VDCN, and CVI exhibited the lowest p-values (Table 3). However, upon performing the MARS model, the most important variables were identified as LSF, TPI, ELE, and VDCN (Figure 10). A similar relationship occurred when evaluating the variables in the datasets of MAX, SUP, BODY, and INF for both the debris flows and debris floods.

The scale of the analyses was adjusted according to the pixel dimension, which, in this case, had a spatial resolution of 5 m. During the inventory elaboration, polygons of variable sizes were observed, which could lead to repeatability when performing segmentation into the four groups, especially in SUP and INF. To mitigate this, in the debris flow inventory, a maximum of two random pixels were chosen to represent the SUP and INF parts of each landslide, and up to a maximum of eight random pixels in BODY. Meanwhile, in the debris floods, the SUP and INF parts were represented with a maximum of 7 pixels and up to a maximum of 63 pixels in BODY.

When comparing the results of the MAX model with SUP in the debris flows, a slight improvement in the SUP models over MAX was evident (Figure 12), suggesting that using at least two pixels to represent the upper part of the landslide could enhance the accuracy of the model. However, this same relationship was not observed in the debris flood inventory (Figure 13), where the MAX models performed relatively better than the SUP models. Nonetheless, the AUC results for both models were not acceptable as they fell below 0.75. This discrepancy could be justified by the smaller size of the debris flood inventory.

5.2. Impact of Sample Size Disparities

It is crucial to highlight the disparity in the number of samples between the debris flows (4316 landslides) and the debris floods (97 mapped landslides). The larger sample size, as in the debris flows, played a crucial role in avoiding biases and ensuring a fair representation of the variable characteristics. This may explain why the IS-lasso model of MAX in debris floods indicated only three significant variables (Figure 8 and Table 3); the smaller sample size could have contributed to less variability in the data. This factor likely adversely affected the performance of the MARS model, which turned out to be poor (AUC < 0.74).

Although the SUP dataset showed more significant variables in the IS-lasso model, it also yielded unsatisfactory results when evaluating the MARS models (AUC < 0.70). In contrast, this phenomenon did not occur with INF, despite using a selection system similar to SUP. The results of the INF models were excellent, reaching an AUC of 0.903. This suggests that, more than the sample size, the heterogeneity of the topographic characteristics significantly contributed to the variability in the model results, especially in the higher part of the landslide.

Nevertheless, the sample size may have affected the accuracy of the models, as evidenced clearly in the AUC graphs (Figures 12 and 13), where there was a higher standard deviation mean in the debris flood models of 0.0544 compared with the standard deviation of the debris flow models of 0.0090.

5.3. Deciphering Variable Importance

Throughout this study, the unique values displayed by variables within each landslide segmentation (MAX, SUP, INF, BODY) underscore the distinct significance of each variable across the segments. This variability was attributed to the distinct topographic features that characterized each landslide zone. Analyzing the segmentation of debris flows, two variables, SLO for initiation zones and LSF for deposit areas, emerged as crucial (Figure 10). The normalized sum of the squared residuals (RSS) accentuated their significance, which made them indispensable for achieving precision in the prediction models.

SLO exhibited a noteworthy difference in means within each segmentation (MAX, SUP, INF, BODY), particularly in MAX, SUP, and BODY segments, where it reached differences of up to four degrees. In contrast, INF exhibited limited capacity to differentiate these areas, with a minimal mean variation of only one degree. This highlights the importance of SLO in MAX, SUP, and BODY but not in INF (Figure 10).

The analysis of LSF revealed its distinguishability in the INF segment, where it showcased a clear disparity between the landslide and non-landslide areas (Figure 17). However, this distinction was less pronounced in BODY and was absent in MAX and SUP, where LSF lacked the ability to discern between landslide and non-landslide areas. In relation to variable importance, ELE stood out for MAX and BODY, while TPI was crucial for SUP and INF (Figure 10). The TPI variable demonstrates a clear differentiation between stable and unstable landslide areas, particularly in INF and SUP (Figure 17), underscoring its crucial role in improving the model precision (Figure 12). On the other hand, elevation (ELE) reveals slight distinguishability, especially in MAX, SUP, and BODY compared to INF. This subtle difference could impact the performance of the MAX and BODY models, in contrast with the performances of INF and SUP using TPI (Figure 12).

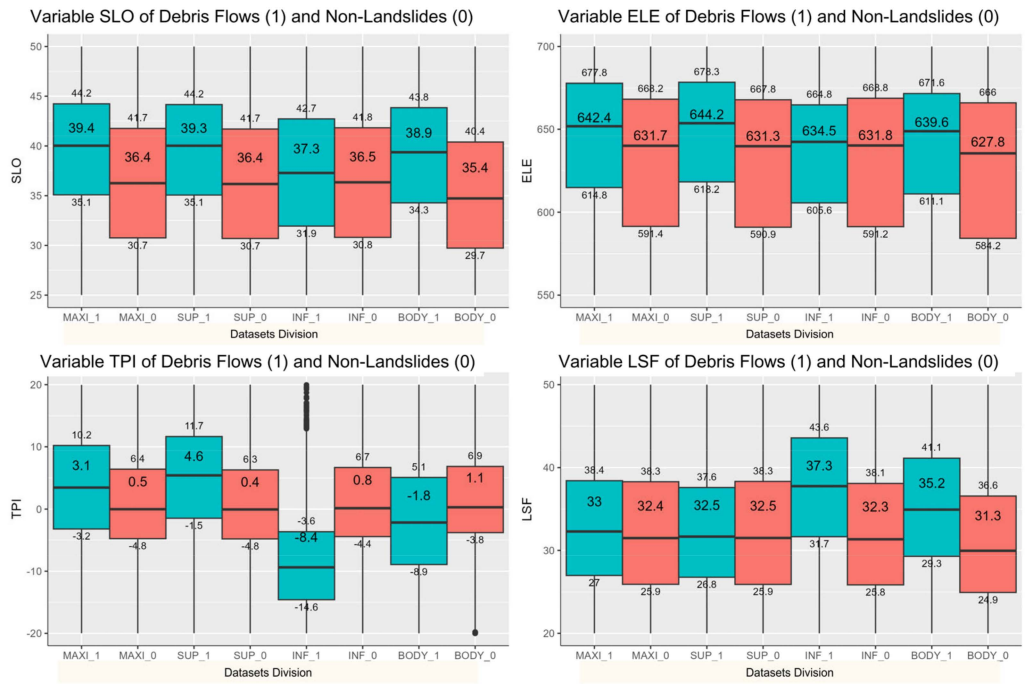

Figure 17. Boxplots illustrating the behavior of the variables SLO, ELE, TPI, and LSF in the MAX, SUP, INF, and BODY segments. Each boxplot displays the data distribution in the groups that represented areas prone to landslides compared with groups without landslides on debris flows.

The lithology also played varying roles across the different segments (Figure 9). For example, more than 74% of the debris flows occurred over the Tierras Blancas Formation (LTL3). The lithology was expected to be among the most important factors to influence

the detachment zones (i.e., MAX and SUP). Surprisingly, lithology ranked as the fourth most influential factor in SUP (Figure 9) but was among the least influential variables in MAX (Figure 10).

In summary, for the debris flow database, the INF model stood out with an AUC value of 0.902 and a standard deviation that ensured accuracy by utilizing the key variables LSF and TPI. It excelled at predicting the deposit extent. For the initiation zones, the models developed with SUP were the most effective and surpassed the MAX model. The BODY model exhibited a lower AUC (0.841) for its segment compared with other models and their respective segments. For example, the MAX model could predict MAX areas with an accuracy of 0.855, while the SUP model achieved an accuracy of 0.856 when predicting SUP areas. On the other hand, the BODY model demonstrated its capability in predicting other segments with values that ranged from 0.762 to 0.785. By contrast, other models, such as the INF model, could not predict SUP areas due to its lower accuracy of 0.58, which was similar to the accuracies of the SUP and MAX models in predicting the INF areas.

When analyzing the most relevant variables for debris floods, only three variables (CVI, SLO, and ELE) were initially identified in the MAX model (Figure 11), which stood out as the only ones capable of distinguishing between the areas prone and not prone to landslides (Figure 8). Although the curvature index (CVI) emerged as the most crucial variable for discerning the areas where landslides initiated, Figure 18 shows that in MAX, the CVI had a mean notably close to areas where landslides did not occur, despite having a larger interquartile range in areas with landslides. Consequently, given the limited number of variables and their restricted ability to reliably distinguish between landslide-prone and non-landslide-prone areas, it is evident that the precision of the MAX model did not reach acceptable levels to predict these areas or others associated with landslides (AUC between 0.654 and 0.74) (Figure 13).

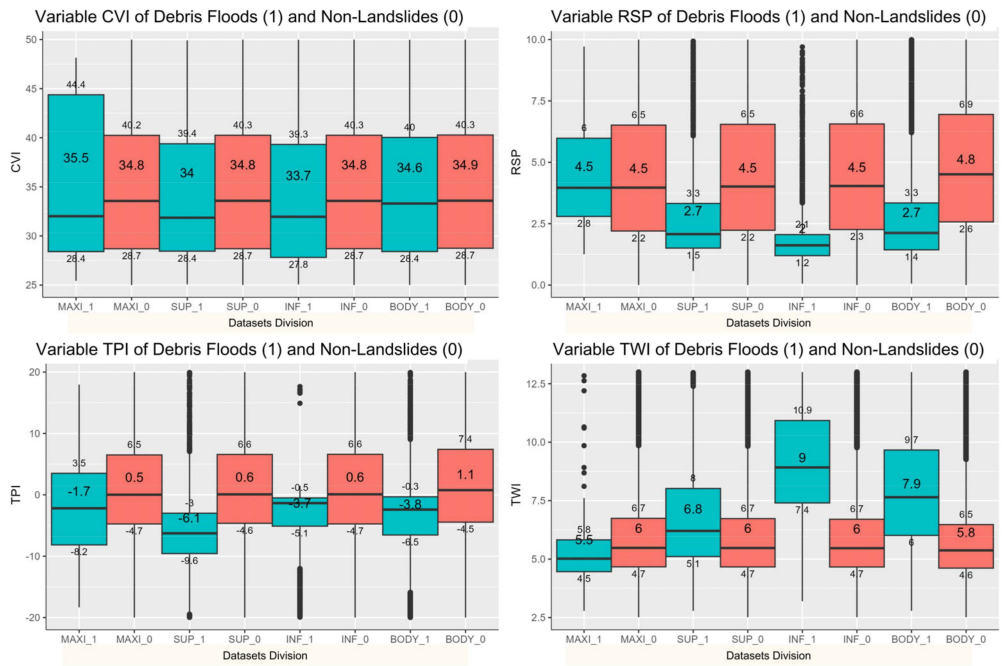

Figure 18. Boxplots illustrating the behavior of the variables CVI, RSP, TPI, and TWI in the MAX, SUP, INF, and BODY segments. Each boxplot displays data distribution in groups representing the areas prone to landslides compared with groups without landslides based on debris floods.

In the case of the SUP model, despite having a greater number of variables to predict the areas prone to landslides, it achieved prediction values (AUC between 0.632 and 0.707) similar to the MAX model. When analyzing two of the most important variables of the

SUP model, RSP and TPI, in Figure 18, it is observed that these variables allowed for differentiation between the areas prone to landslides and those that were not. Despite having variables capable of distinguishing areas where landslides may initiate based on their sets of discriminatory values, it is plausible that the limited number of samples, i.e., the restricted inventory obtained from the area, played a crucial role in the predictive capacity of the models. This phenomenon may also be attributed to the fact that the shape of a debris flood covers a larger deposition area. Therefore, since SUP selects the top 10% of pixels, it is possible that this 10% may have included features not exclusive to the upper part but also to the middle part of the landslide.

In contrast, the INF models demonstrated outstanding results in predicting deposition areas (AUC 0.903) and identifying the area of landslides (AUC 0.913). From this perspective, the predictive capacity of the INF model (AUC 0.913) was significantly higher compared with the BODY model (AUC 0.815) for forecasting the entire extent affected by a landslide (BODY dataset). This suggests that this type of landslide tended to exhibit a wide extension in its deposits, and by focusing on these characteristics, it may not effectively contribute to predicting other related areas, such as initiation zones.

When evaluating the most relevant variables of INF, such as RSP, TWI, and TPI (Figure 11), it is evident that these variables served excellently to differentiate between the areas affected by landslides and those that were not. This can be observed in the boxplot of these three variables (Figure 18), where a clear distinction in values was apparent between the debris flood group and stable areas without landslides. Finally, the BODY model also demonstrated a reliable capability to predict the extension areas of debris floods (AUC BODY 0.815), including the locations of their deposits (AUC INF 0.801).

Finally, when comparing the standard deviations obtained in the models for the debris floods (SD M.BODY 0.013) with the debris flows (SD M.BODY 0.005), it was observed that the former exhibited lower precision, as indicated by a higher standard deviation, which was a pattern also evident in other models (Tables 4 and 5). Additionally, it could be concluded that the limited sample size and the disparity in the terrain characteristics between the upper and lower parts, where the deposit occurred, could impact the prediction of less covered areas, such as the initiation zones.

5.4. Comparing Results with Similar Studies

In the experiments conducted on the debris flows, it was observed that the SUP models exhibited a higher accuracy (AUC of 0.860 and 0.858) compared with the MAX models (AUC of 0.855 and 0.853) in predicting areas prone to initiate landslides (Figure 12). These findings aligned with those of Regmi et al. (2014) [12], who emphasized that model accuracy is inherently linked to the sampling technique. According to his findings, landslides sampled as areas, in line with the approach similar to SUP, demonstrated superior accuracy (85%) compared with models based on landslides sampled as a single point, which exhibited an accuracy of 83%. This study confirmed that area-based sampling strategies, such as those used in SUP models, enhance the predictive performance for initiation zones.

Magliulo et al. (2008) [11] conducted sampling experiments by performing two segmentations: one corresponded to the source area, similar to SUP, and the other involved the polygon of the entire landslide body, somewhat similar to BODY in the current study. Based on their results, models obtained in detachment zones proved to be more reliable compared with areas that encompassed the entire landslide body. Therefore, upon assessing the results of the SUP and BODY models in debris flows, it was observed that the SUP models exhibited a higher accuracy in delineating source areas (AUC 0.860) compared with BODY models in identifying zones that comprised the entire landslide body (AUC 0.841)

(Figure 12). These findings highlight that focusing on specific landslide segments improves the prediction accuracy.

Additionally, Vorpahl et al. (2012) [13], who conducted the segmentation of landslides into three areas—initiation, transport, and deposition—demonstrated that models that predicted deposition areas outperformed those that predicted detachment zones. Similarly, upon reviewing the results for both the debris flows and debris floods in this study, the INF models achieved a superior accuracy (AUC 0.902 for the debris flows and 0.903 for the debris floods) compared with the SUP models (AUC 0.858 and 0.706) and MAX models (AUC 0.855 and 0.738). This result underscores the importance of depositional zones for understanding material redistribution processes and improving hazard mitigation strategies.

However, unlike previous studies, such as Vorpahl et al. (2012) [13] and Vargas-Cuervo et al. (2019) [9], which primarily focused on evaluating the model accuracy within the same landslide segment used for training, this study took a distinctive approach by cross-evaluating the models across different segments. Specifically, we trained models on one part of a landslide (e.g., SUP) and tested them on another part (e.g., INF). This cross-application strategy revealed critical insights: while models trained on source zones, like SUP, performed well at predicting initiation zones, they struggled to predict depositional zones, such as INF, accurately (AUC < 0.60). This finding highlights a key limitation in using single-segment inventories for comprehensive susceptibility mapping and underscores the necessity of tailored approaches for each segment.

The identification of key variables also aligned with findings from previous studies while highlighting unique contributions from this research. For example, SLO and ELE were identified as significant variables in the MAX models of debris flows in this study and were similarly highlighted by Catani et al. (2013) [57] and Reichenbach et al. (2018) [58], both of which utilized MARS methods for landslide susceptibility modeling. Furthermore, Regmi et al. (2014) [12] emphasized SLO, ELE, and curvature as predominant variables for distinguishing landslides, while Magliulo et al. (2008) [11] indicated that SLO combined with lithology plays an influential role in predicting detachment zones.

To identify depositional landslide areas (INF models) in the debris flow database, the LS factor (LSF), topographic position index (TPI), and elevation (ELE) were the most influential variables. Meanwhile, in the debris flood database, the most crucial variables were relative slope position (RSP), TWI, TPI, and Steam Power Index (SPI). These findings aligned with the results of Vorpahl et al. (2012) [13], who observed SPI, TWI, and TPI as the most important variables for distinguishing landslide deposition zones.

The effectiveness of models based on deposition area data (INF), as demonstrated in this study, highlights the critical role of incorporating the distinct characteristics of deposition zones in landslide susceptibility modeling. These zones often exhibit unique topographic features, such as gentler slopes, concave landforms, and proximity to drainage channels, which influence the accumulation and distribution of landslide debris. These features may not be adequately captured by models that focus solely on the initiation zones or the entire landslide body. By specifically targeting deposition zones, our INF model effectively incorporates these unique characteristics, resulting in a more accurate prediction of landslide deposit areas. This enhanced accuracy can have significant implications for hazard assessment and mitigation, as it enables the more precise identification of areas at risk from landslide impacts.

6. Concluding Remarks

This study evaluated landslide susceptibility by comparing models trained and tested on inventories derived from different parts of landslides (MAX, SUP, INF, BODY) and identifying the most relevant variables for predicting depositional zones and other landslide-

affected areas. Our research examined the cross-applicability of models trained on one landslide component and tested on another, and not only the performance of models trained and tested on the same parts of landslides. The results demonstrate that segmentation strategies are critical for improving the model accuracy and understanding the spatial variability of landslide processes.

The findings highlight that INF models consistently outperformed other models for both the debris flows (AUC 0.902) and the debris floods (AUC 0.903), underscoring the importance of focusing on depositional zones for hazard mitigation. Key variables, such as the LS factor (LSF), topographic position index (TPI), and relative slope position (RSP), proved to be highly influential for predicting depositional areas, while slope (SLO) and elevation (ELE) were more relevant for the initiation zones.

A key innovation of this study lies in its cross-application strategy, where models trained on one landslide segment (e.g., SUP) were tested on another segment (e.g., INF). This approach revealed critical limitations in single-segment inventories: models trained exclusively on source zones, like SUP, performed poorly when applied to predict depositional zones, such as INF (AUC < 0.60). This finding underscores the need for tailored approaches that account for the unique characteristics of each segment to ensure comprehensive susceptibility mapping. Unlike previous studies, such as Vorpahl et al. (2012) [13] and Vargas-Cuervo et al. (2019) [9], which explored how the model accuracy changes when training and testing are performed on different parts of a landslide but always applied the models to predict the same part used for training, our study demonstrated that cross-application strategies provide deeper insights into the transferability of models across segments.

The IS-Lasso method was instrumental in identifying significant variables across datasets, which enabled an initial ranking of predictors based on their statistical importance. However, this study also demonstrated that variable importance rankings derived from IS-Lasso may differ from those identified during predictive modeling with MARS. This highlights the complementary nature of these methods and their combined utility in improving landslide susceptibility assessments.

This study also revealed notable differences between debris flows and debris floods in terms of the sample size and predictive performance. The debris flows benefited from a larger sample size (4316 landslides), which led to a more robust model performance with lower standard deviations across the AUC values. In contrast, the debris floods had a much smaller sample size (97 mapped landslides), resulting in a higher variability in the model performance and lower predictive accuracy for some inventories. Despite these limitations, the INF models still demonstrated excellent predictive performance for depositional zones in both the debris flow and debris flood datasets. These results suggest that the heterogeneity in the topographic characteristics played a more significant role than the sample size alone in determining the model outcomes.

The findings may have important implications for disaster risk reduction policies and land-use planning. Hazard mitigation efforts should prioritize depositional zones due to their direct impact on human settlements and infrastructure. Authorities should also consider adopting cross-segment modeling approaches to ensure comprehensive hazard assessments that address the limitations of single-segment inventories.

From a practical perspective, this study provides insights that can enhance early warning systems by identifying key variables, such as LSF, TPI, and RSP, to improve susceptibility maps' accuracy. Predictive models focused on depositional zones can also guide infrastructure development to minimize exposure to landslide risks.

Future research should explore whether cross-segment modeling approaches are transferable to other regions with varying geomorphological conditions. Expanding datasets for

underrepresented phenomena, like debris floods, would also improve the model robustness and reduce the variability in the performance metrics.

In conclusion, this study advanced our understanding of landslide dynamics by introducing innovative segmentation strategies and cross-application modeling approaches and combining statistical methods, like IS-Lasso, with machine learning techniques, like MARS. These findings provide a foundation for more accurate hazard assessments and effective mitigation strategies in landslide-prone areas worldwide.

Author Contributions: Conceptualization, L.P.C.-C. and C.C.; methodology: L.P.C.-C.; software: L.P.C.-C., C.M. (Chiara Martinello) and C.M. (Claudio Mercurio); validation: L.P.C.-C., T.F. and C.C.; formal analysis: L.P.C.-C.; investigation: L.P.C.-C.; resources: L.P.C.-C. and A.A.A.-P.; data curation: L.P.C.-C., A.A.A.-P., C.M. (Chiara Martinello) and C.M. (Claudio Mercurio); writing—original draft preparation: L.P.C.-C.; writing—review and editing: L.P.C.-C., T.F., E.R. and C.C.; visualization: L.P.C.-C.; supervision: E.R., T.F. and C.C.; project administration: C.C; funding acquisition: C.C. All authors have read and agreed to the published version of the manuscript.

Funding: This research was funded by the Italian Agency for Development Cooperation (AICS) as part of the project "Establecer y desarrollar la carrera de Licenciatura en Ciencias de la Tierra con énfasis en Geología en la Universidad de El Salvador (CASTES)" (AID 11726), scientific responsible Christian Conoscenti (University of Palermo).

Data Availability Statement: The data are available from the corresponding author upon reasonable request.

Acknowledgments: The authors thank the editor and reviewers for their valuable contributions to this manuscript.

Conflicts of Interest: The authors declare no conflicts of interest.

References

1. Brabb, E.E. Innovative Approaches to Landslide Hazard Mapping. In Proceedings of the 4th International Symposium on Landslides, Toronto, ON, Canada, 16–21 September 1984; Volume 1, pp. 307–324.
2. Guzzetti, F.; Carrara, A.; Cardinali, M.; Reichenbach, P. Landslide hazard evaluation: A review of current techniques and their application in a multi-scale study, Central Italy. *Geomorphology* **1999**, *31*, 181–216. [CrossRef]
3. Guzzetti, F. Landslide Hazard and Risk Assessment. Rheinische Friedrich-Wilhelms-Universität. 2005. Available online: https://geomorphology.irpi.cnr.it/Members/fausto/PhD-dissertation/Landslide_Hazard_and_Risk_Assessment.pdf (accessed on 15 June 2023).
4. Lima, P.; Steger, S.; Glade, T. Counteracting flawed landslide data in statistically based landslide susceptibility modelling for very large areas: A national-scale assessment for Austria. *Landslides* **2021**, *18*, 3531–3546. [CrossRef]
5. Heckmann, T.; Gegg, K.; Gegg, A.; Becht, M. Sample size matters: Investigating the effect of sample size on a logistic regression susceptibility model for debris flows. *Nat. Hazards Earth Syst. Sci.* **2014**, *14*, 259–278. [CrossRef]
6. Heckmann, T.; Becht, M. Investigating the transferability of statistical disposition models for slope-type debris flows. *Erdkunde* **2009**, *63*, 19–33. [CrossRef]
7. Remondo, J.; González-Díez, A.; Ramón, J.; de Terán, D.; Cendrero, A. Landslide Susceptibility Models Utilising Spatial Data Analysis Techniques. A Case Study from the Lower Deba Valley, Guipúzcoa (Spain). *Nat. Hazards* **2003**, *30*, 267–279. [CrossRef]
8. van den Eeckhaut, M.; Vanwalleghem, T.; Poesen, J.; Govers, G.; Verstraeten, G.; Vandekerckhove, L. Prediction of landslide susceptibility using rare events logistic regression: A case-study in the Flemish Ardennes (Belgium). *Geomorphology* **2006**, *76*, 392–410. [CrossRef]
9. Vargas-Cuervo, G.; Rotigliano, E.; Conoscenti, C. Prediction of debris-avalanches and -flows triggered by a tropical storm by using a stochastic approach: An application to the events occurred in Mocoa (Colombia) on 1 April 2017. *Geomorphology* **2019**, *339*, 31–43. [CrossRef]
10. Dou, J.; Yunus, A.P.; Merghadi, A.; Shirzadi, A.; Nguyen, H.; Hussain, Y.; Avtar, R.; Chen, Y.; Pham, B.T.; Yamagishi, H. Different sampling strategies for predicting landslide susceptibilities are deemed less consequential with deep learning. *Sci. Total Environ.* **2020**, *720*, 137320. [CrossRef]
11. Magliulo, P.; di Lisio, A.; Russo, F.; Zelano, A. Geomorphology and landslide susceptibility assessment using GIS and bivariate statistics: A case study in southern Italy. *Nat. Hazards* **2008**, *47*, 411–435. [CrossRef]

12. Regmi, N.R.; Giardino, J.R.; McDonald, E.V.; Vitek, J.D. A comparison of logistic regression-based models of susceptibility to landslides in western Colorado, USA. *Landslides* **2014**, *11*, 247–262. [CrossRef]
13. Vorpahl, P.; Elsenbeer, H.; Märker, M.; Schröder, B. How can statistical models help to determine driving factors of landslides? *Ecol. Model.* **2012**, *239*, 27–39. [CrossRef]
14. Conoscenti, C.; Ciaccio, M.; Caraballo-Arias, N.A.; Gómez-Gutiérrez, Á.; Rotigliano, E.; Agnesi, V. Assessment of susceptibility to earth-flow landslide using logistic regression and multivariate adaptive regression splines: A case of the Belice River basin (western Sicily, Italy). *Geomorphology* **2015**, *242*, 49–64. [CrossRef]
15. Hong, H.; Liu, J.; Bui, D.T.; Pradhan, B.; Acharya, T.D.; Pham, B.T.; Zhu, A.X.; Chen, W.; Ahmad, B. Bin. Landslide susceptibility mapping using J48 Decision Tree with AdaBoost, Bagging and Rotation Forest ensembles in the Guangchang area (China). *Catena* **2018**, *163*, 399–413. [CrossRef]
16. Martinello, C.; Cappadonia, C.; Conoscenti, C.; Agnesi, V.; Rotigliano, E. Optimal slope units partitioning in landslide susceptibility mapping. *J. Maps* **2021**, *17*, 152–162. [CrossRef]
17. Alonso-Henar, J.; Álvarez-Gómez, J.A.; Martínez-Díaz, J.J. Neogene-quaternary evolution from transpressional to transtensional tectonics in Northern Central America controlled by cocos: Caribbean subduction coupling change. *J. Iber. Geol.* **2017**, *43*, 519–538. [CrossRef]
18. Suñe-Puchol, I.; Aguirre-Díaz, G.J.; Dávila-Harris, P.; Miggins, D.P.; Pedrazzi, D.; Costa, A.; Ortega-Obregón, C.; Lacan, P.; Hernández, W.; Gutiérrez, E. The Ilopango caldera complex, El Salvador: Origin and early ignimbrite-forming eruptions of a graben/pull-apart caldera structure. *J. Volcanol. Geotherm. Res.* **2019**, *371*, 1–19. [CrossRef]
19. DeMets, C. A new estimate for present-day Cocos-Caribbean plate motion: Implications for slip along the Central American volcanic arc. *Geophys. Res.* **2001**, *28*, 4043–4046. [CrossRef]
20. Dixon, T. GPS measurement of relative motion of the Cocos and Caribbean plates and strain accumulation across the Middle America trench. *Geophys. Res.* **1993**, *20*, 2167–2170. Available online: https://agupubs.onlinelibrary.wiley.com/doi/abs/10.1029/93GL02415 (accessed on 2 May 2023). [CrossRef]
21. Martínez-Díaz, J.; Alvarez-Gómez, J.; Benito, B.; Hernández, D. Triggering of destructive earthquakes in El Salvador. *Geology* **2004**, *32*, 65–68. Available online: https://pubs.geoscienceworld.org/ssa/geology/article/32/1/65/129218 (accessed on 2 May 2023). [CrossRef]
22. Agostini, S.; Corti, G.; Doglioni, C.; Carminati, E.; Innocenti, F.; Tonarini, S.; Montanari, D. Tectonic and magmatic evolution of the active volcanic front in El Salvador: Insight into the Berlín and Ahuachapán geothermal areas. *Geothermics* **2006**, *35*, 368–408. [CrossRef]
23. Canora, C.; Villamor, P.; Martínez-Díaz, J.J.; Berryman, K.R.; Álvarez-Gómez, J.A.; Capote, R.; Hernández, W. Paleoseismic analysis of the San Vicente segment of the El Salvador Fault Zone, El Salvador, Central America. *Geol. Acta* **2012**, *10*, 103–123. Available online: https://www.redalyc.org/pdf/505/50524522002.pdf (accessed on 2 May 2023).
24. Corti, G.; Carminati, E.; Mazzarini, F.; Garcia, M.O. Active strike-slip faulting in El Salvador, central America. *Geology* **2005**, *33*, 989–992. [CrossRef]
25. Funk, J.; Mann, P.; McIntosh, K.; Stephens, J. Cenozoic tectonics of the Nicaraguan depression, Nicaragua, and Median Trough, El Salvador, based on seismic-reflection profiling and remote-sensing data. *Geol. Soc. Am. Bull.* **2009**, *121*, 1491–1521. Available online: https://pubs.geoscienceworld.org/gsa/gsabulletin/article-abstract/121/11-12/1491/2345 (accessed on 2 May 2023). [CrossRef]
26. Calderón-Cucunubá, L.P. El uso de la Geomática en la Caracterización Geométrica y Morfológica de la Caldera de Ilopango, "República del Salvador". Master's Dissertation, Universidad Autónoma de San Luis de Potosí, San Luis Potosí, Mexico, 2018. Available online: https://repositorioinstitucional.uaslp.mx/xmlui/bitstream/handle/i/5686/Tesis_Laura%20Paola%20Calderon%20Cucunuba%20(1).pdf?sequence=1&isAllowed=y (accessed on 2 May 2023).
27. Suñe-Puchol, I.; Aguirre-Díaz, G.J.; Pedrazzi, D.; Dávila-Harris, P.; Miggins, D.P.; Costa, A.; Ortega-Obregón, C.; Lacan, P.; Gutierrez, E.; Hernández, W. The Ilopango caldera complex, El Salvador: Stratigraphic revision of the complete eruptive sequence and recurrence of large explosive eruptions. *J. Volcanol. Geotherm. Res.* **2019**, *374*, 100–119. [CrossRef]
28. Kattan, C.; Menjívar, L.; Molina, G.; Peñate, Y.; Estrada, A.; Moran, I.; Cañas, A. Informe Nacional del Estado de los Riesgos y Vulnerabilidades. Ministerio de Medio Ambiente y Recursos Naturales (MARN). 2017. Available online: https://srt.snet.gob.sv/tallerdivulgacion/RiesgoSismico/1.%20Informe%20Nacional%20del%20Estado%20de%20los%20Riesgos%20y%20Vulnerabilidad-%202017.pdf (accessed on 2 May 2023).
29. Rabby, Y.W.; Li, Y. An integrated approach to map landslides in Chittagong Hilly Areas, Bangladesh, using Google Earth and field mapping. *Landslides* **2019**, *16*, 633–645. [CrossRef]
30. Costanzo, D.; Chacón, J.; Conoscenti, C.; Irigaray, C.; Rotigliano, E. Forward logistic regression for earth-flow landslide susceptibility assessment in the Platani river basin (southern Sicily, Italy). *Landslides* **2014**, *11*, 639–653. [CrossRef]

31. Rotigliano, E.; Martinello, C.; Hernandéz, M.A.; Agnesi, V.; Conoscenti, C. Predicting the landslides triggered by the 2009 96E/Ida tropical storms in the Ilopango caldera area (El Salvador, CA): Optimizing MARS-based model building and validation strategies. *Environ. Earth Sci.* **2019**, *78*, 210. [CrossRef]
32. Conrad, O.; Bechtel, B.; Bock, M.; Dietrich, H.; Fischer, E.; Gerlitz, L.; Wehberg, J.; Wichmann, V.; Böhner, J. System for Automated Geoscientific Analyses (SAGA) v. 2.1.4. *Geosci. Model Dev.* **2015**, *8*, 1991–2007. [CrossRef]
33. Weber, H.S.; Wiesemann, G.; Wittekindt, H. *Mapa Geológico General de la República de El Salvador 1:500,000/Geologische Übersichtskarte der Republik El Salvador 1:500,000 (After Geological Maps 1:100,000-1967-74)-Bundesanstalt für Bodenforschung*; Bundesanstalt für Bodenforschung: Hannover, Germany, 1974.
34. Rouse, J.W., Jr.; Haas, R.H.; Schell, J.A.; Deering, D.W. Third Earth Resources Technology Satellite-1 Symposium. In Proceedings of the Third Symposium on Significant Results Obtained from the first Earth Resources, Washington, DC, USA, 10–14 December 1973; Goddard Space Flight Center, Scientific and Technical Information Office, National Aeronautics and Space Administration: Washington, DC, USA, 1974; Volume 351, p. 309.
35. Jackson, R.D.; Huete, A.R. Interpreting vegetation indices. *Prev. Vet. Med.* **1991**, *11*, 185–200. [CrossRef]
36. Zevenbergen, L.W.; Thorne, C.R. Quantitative analysis of land surface topography. *Earth Surf. Process. Landf.* **1987**, *12*, 47–56. [CrossRef]
37. Dikau, R. Entwurf einer geomorphographisch-analytischen Systematik von Reliefeinheiten. *Heidelb. Geogr. Bausteine* **1988**, *5*, 45.
38. Shary, P.A. Land surface in gravity points classification by a complete system of curvatures. *Math. Geol.* **1995**, *27*, 373–390. [CrossRef]
39. Hengl, T.; Reuter, H.I. (Eds.) *Geomorphometry: Concepts, Software, Applications, Developments in Soil Science*; Elsevier: Amsterdam, The Netherlands, 2008; Volume 33.
40. Shary, P.A.; Sharaya, L.S.; Mitusov, A.V. Fundamental quantitative methods of land surface analysis. *Geoderma* **2002**, *107*, 1–32. [CrossRef]
41. Köthe, R.; Gehrt, E.; Böhner, J. Automatische Reliefanalyse für geowissenschaftliche Anwendungen-derzeitiger Stand und Weiterentwicklungen des Programms SARA. *Arbeitshefte Geol.* **1996**, *1*, 31–37.
42. Watkins, R.L. Terrain Metrics and Landscape Characterization from Bathymetric Data: SAGA GIS Methods and Command Sequences. 2019. Available online: https://ftp.soest.hawaii.edu/pibhmc/website/webdocs/documentation/linkages_project_methods_final.pdf (accessed on 10 July 2023).
43. Desmet, P.J.J.; Govers, G. A GIS procedure for automatically calculating the USLE LS factor on topographically complex landscape units. *J. Soil Water Conserv.* **1996**, *51*, 427–433. Available online: https://www.jswconline.org/content/51/5/427.short (accessed on 10 July 2023).
44. Bock, M.; Böhner, J.; Conrad, O.; Köthe, R.; Ringeler, A. XV. Methods for creating functional soil databases and applying digital soil mapping with SAGA GIS. *JRC Sci. Tech. Rep.* **2007**, 149–163. Available online: https://www.researchgate.net/publication/267706527_XV_Methods_for_creating_Functional_Soil_Databases_and_applying_Digital_Soil_Mapping_with_SAGA_GIS (accessed on 10 July 2023).
45. Gruber, S.; Peckham, S. Chapter 7 Land-Surface Parameters and Objects in Hydrology. *Dev. Soil Sci.* **2009**, *33*, 171–194. [CrossRef]
46. Quinn, P.F.; Beven, K.J.; Lamb, R. The in(a/tan/β) index: How to calculate it and how to use it within the topmodel framework. *Hydrol. Process.* **1995**, *9*, 161–182. [CrossRef]
47. Riley, S.J.; DeGloria, S.D.; Elliot, R. Index that quantifies topographic heterogeneity. *Intermt. J. Sci.* **1999**, *5*, 23–27.
48. Weiss, A. Topographic position and landforms analysis. Poster Presentation. In Proceedings of the ESRI User Conference, San Diego, CA, USA, 9–13 July 2001; Volume 64, pp. 227–245.
49. Bock, M.; Köthe, R. Predicting the depth of hydromorphic soil characteristics influenced by ground water. *SAGA Second. Out* **2008**, *19*, 13–22. Available online: https://www.researchgate.net/publication/267553405 (accessed on 10 July 2023).
50. Hungr, O.; Leroueil, S.; Picarelli, L. The Varnes classification of landslide types, an update. *Landslides* **2014**, *11*, 167–194. [CrossRef]
51. Cilluffo, G.; Sottile, G.; La Grutta, S.; Muggeo, V.M.R. The Induced Smoothed lasso: A practical framework for hypothesis testing in high dimensional regression. *Stat. Methods Med. Res.* **2020**, *29*, 765–777. [CrossRef] [PubMed]
52. R Core Team. R: A Language and Environment for Statistical Computing (R-4.3.1). R Foundation for Statistical Computing. 2021. Available online: https://www.R-project.org/ (accessed on 10 July 2023).
53. Friedman, J.H. Estimating Functions of Mixed Ordinal and Categorical Variables Using Adaptive Splines. 1991. Available online: https://apps.dtic.mil/sti/citations/ADA590939 (accessed on 10 July 2023).
54. Chung, C.J.F.; Fabbri, A.G. Validation of spatial prediction models for landslide hazard mapping. *Nat. Hazards* **2003**, *30*, 451–472. [CrossRef]
55. Tien Bui, D.; Tuan, T.A.; Klempe, H.; Pradhan, B.; Revhaug, I. Spatial prediction models for shallow landslide hazards: A comparative assessment of the efficacy of support vector machines, artificial neural networks, kernel logistic regression, and logistic model tree. *Landslides* **2016**, *13*, 361–378. [CrossRef]

56. Milborrow, S. Notes on the Earth Package. 2021. Available online: http://mtweb.cs.ucl.ac.uk/mus/lib/R/earth/doc/earth-notes.pdf (accessed on 10 July 2023).
57. Catani, F.; Lagomarsino, D.; Segoni, S.; Tofani, V. Landslide susceptibility estimation by random forests technique: Sensitivity and scaling issues. *Nat. Hazards Earth Syst. Sci.* **2013**, *13*, 2815–2831. [CrossRef]
58. Reichenbach, P.; Rossi, M.; Malamud, B.D.; Mihir, M.; Guzzetti, F. A review of statistically-based landslide susceptibility models. *Earth Sci. Rev.* **2018**, *180*, 60–91. [CrossRef]

Disclaimer/Publisher's Note: The statements, opinions and data contained in all publications are solely those of the individual author(s) and contributor(s) and not of MDPI and/or the editor(s). MDPI and/or the editor(s) disclaim responsibility for any injury to people or property resulting from any ideas, methods, instructions or products referred to in the content.